

The Formation of the First Quasars. I. The Black Hole Seeds, Accretion and Feedback Models

Qirong Zhu¹★, Yuexing Li^{2,3,4}, Yiting Li⁵, Moupiya Maji⁶, Hidenobu Yajima⁷, Raffaella Schneider^{4,8}, and Lars Hernquist⁹

¹ Department of Physics, Carnegie Mellon University, 5000 Forbes Avenue, Pittsburgh, PA 15213, USA

² Department of Astronomy & Astrophysics, The Pennsylvania State University, University Park, PA 16802, USA

³ Institute for Cosmology and Gravity, The Pennsylvania State University, University Park, PA 16802, USA

⁴ Dipartimento di Fisica, Sapienza, Università di Roma, Piazzale Aldo Moro 5, 00185, Roma, Italy

⁵ Department of Physics, University of California, Santa Barbara, CA 94720, USA

⁶ Observatoire de Genève, Chemin des Maillettes, 51, 1290 Versoix, Switzerland

⁷ Center for Computational Sciences University of Tsukuba, Tsukuba, Ibaraki 305-8577, Japan

⁸ INFN, Sezione di Roma I, P.le Aldo Moro 2, 00185 Roma, Italy

⁹ Harvard-Smithsonian Center for Astrophysics, Harvard University, 60 Garden Street, Cambridge, MA 02138, USA

Accepted XXX. Received YYY; in original form ZZZ

ABSTRACT

Supermassive black holes (SMBHs) of $\sim 10^9 M_\odot$ are generally believed to be the central engines of the luminous quasars observed at $z \gtrsim 6$, but their astrophysical origin remains elusive. The $z \gtrsim 6$ quasars reside in rare density peaks, which poses several challenges to uniform hydrodynamic simulations. To investigate the formation of these distant quasars, we perform a suite of zoom-in simulations on a favorable halo, with a mass of $\sim 10^{13} M_\odot$ at $z = 6$ and a history of multiple major mergers, ideal for BH growth. We test BH seeds of $10 - 10^6 M_\odot$, and various accretion and feedback models, including thin-disk and slim-disk accretion. We find, contrary to previous studies, that light seeds of $\lesssim 10^3 M_\odot$ fail to grow to $10^8 M_\odot$ by $z \sim 6$ even with super-critical accretion; that the hyper-Eddington mode leads to lower accretion rates than the Eddington-limited case due to stronger feedback, resulting in significantly smaller BHs by two orders of magnitude; and that while the super-critical model boosts the growth of low-spin BHs, for high-spin BHs the mass may be reduced due to increased radiative feedback. Our simulations show that the first $10^8 - 10^9 M_\odot$ SMBHs may grow from heavy seeds of $\gtrsim 10^4 M_\odot$ via Eddington-limited or mild super-critical accretion facilitated by gas-rich mergers and self-regulated by feedback, and they co-evolve with their host galaxies, producing bright quasars such as those at $z \sim 6$ and ULAS J1342+0928, currently the most distant quasar at $z = 7.54$.

Key words: the first quasars – quasars: supermassive black holes – black hole physics – galaxies: high-redshift – galaxies: formation – galaxies: evolution – cosmology: theory

1 INTRODUCTION

Over the last two decades, more than 200 quasars have been discovered at high redshift $z \gtrsim 6$ (e.g., Fan et al. 2001; Willott et al. 2010; Venemans et al. 2015; Jiang et al. 2016; Bañados et al. 2016; Reed et al. 2017; Matsuoka et al. 2018; Shen et al. 2019), among them a handful are at $z > 7$ (e.g., Mortlock et al. 2011; Matsuoka et al. 2019; Wang et al. 2019; Yang et al. 2019), with the record-holder of the most distant quasar being at $z = 7.54$ (Bañados et al. 2018; Yang et al. 2020) when the age of Universe is less than 700 Myr (e.g., see a recent review by Inayoshi et al. 2020).

Multi-band observations suggest that these quasars are powered by supermassive black holes (SMBHs) of mass $\sim 10^8 - 10^9 M_\odot$, with the most massive of all, SDSS J0100+2802, having an estimated mass of $1.2 \times 10^{10} M_\odot$ at $z = 6.3$ (Wu et al. 2015), while the two most distant ones, ULAS J1342+0928 and the recently reported *Pōniuā’ena* (J1007+2115, Yang et al. 2020), having a mass of $7.8 \times 10^8 M_\odot$ at $z = 7.54$ (Bañados et al. 2018), and $1.5 \times 10^9 M_\odot$ at $z = 7.52$ (Yang et al. 2020), respectively.

Furthermore, the observations suggest that these SMBHs accrete at sub- or near-Eddington rates (e.g., Willott et al. 2010; Mazzucchelli et al. 2017; Onoue et al. 2019; Shen et al. 2019; Vito et al. 2019). Shen et al. (2019) reported a median value of the Eddington ratio $\lambda_{\text{Edd}} \sim 0.3$ for a sample of 50 $z > 5.7$ quasars, while Maz-

★ E-mail: qirongz@andrew.cmu.edu

zucchelli et al. (2017) found an average $\lambda_{\text{Edd}} \sim 0.4$ at $z \gtrsim 6.5$, and Vito et al. (2019) reported the a range of $0.2 - 1.76$ for a sample of 21 $z > 6$ quasars. More recently, Davies et al. (2019) suggested that the $z > 7$ quasars may have high accretion rates without violating the Eddington limit due to low radiative efficiency.

These extraordinary observations raise fundamental questions about the origin and the rapid formation of $\sim 10^8 - 10^{10} M_{\odot}$ SMBHs within the first billion years after the Big Bang: what were the BH seeds? And, how did they grow?

Unlike stellar mass black holes, the origin of SMBHs is much less well understood. In recent years, three major seed scenarios have been proposed (see reviews by Volonteri 2010; Volonteri & Bellovary 2012; Latif & Ferrara 2016; Woods et al. 2019, and more recently by Greene et al. 2020): (1) light seeds $\sim 10^{1-2} M_{\odot}$ from Pop III stars (e.g., Madau et al. 2014; Lupi et al. 2016; Ryu et al. 2016; Valiante et al. 2016, 2017; Pezzulli et al. 2016, 2017); (2) intermediate seeds of $\sim 10^{3-4} M_{\odot}$ from the collapse of super-massive stars (e.g., Ferrara et al. 2014; Woods et al. 2017, 2019) or stellar collisions (e.g., Katz et al. 2015; Yajima & Khochfar 2016; Sakurai et al. 2017; Tagawa et al. 2020); and (3) heavy seeds of $\sim 10^{5-6} M_{\odot}$ from the collapse of hot and dense gas clumps, so-called direct collapse black holes (DCBHs) (e.g., Agarwal et al. 2012; Glover 2015a,b; Pacucci et al. 2015; Inayoshi & Haiman 2016; Valiante et al. 2016; Regan et al. 2017; Chon et al. 2018; Regan et al. 2019; Wise et al. 2019; Luo et al. 2020).

The rapid growth of the BH seeds, on the other hand, poses yet another long-standing challenge. Assuming the seeds grow at Eddington-limited accretion, the timescale for a seed to grow from M_{seed} to a given BH mass M_{BH} is given by (e.g., Soltan 1982; Woods et al. 2019; Inayoshi et al. 2020):

$$t_{\text{grow}} \approx \frac{0.45}{f_{\text{duty}}} \frac{\epsilon_r}{(1 - \epsilon_r)} \ln \left(\frac{M_{\text{BH}}}{M_{\text{seed}}} \right) \text{ Gyr}, \quad (1)$$

where f_{duty} is the duty cycle of Eddington accretion, and ϵ_r is the radiative efficiency. Assuming a radiatively-efficient, thin-disk accretion model (Shakura & Sunyaev 1973) with $\epsilon_r = 0.1$, a seed will grow exponentially with an e-folding time of ~ 50 Myr. So for $100 M_{\odot}$ BH seeds from Pop III stars, constant accretion at the Eddington rate with a full duty cycle ($f_{\text{duty}} = 1$), ~ 810 Myr are required to grow to $10^9 M_{\odot}$.

In reality, it may be difficult to achieve such an ideal growth scenario as many simulations have shown inefficient accretion onto Pop III remnants due to strong radiative feedback (e.g., Alvarez et al. 2009; Jeon et al. 2012; Tanaka et al. 2012; Smith et al. 2018). To decrease the growth timescale, a number of solutions have been proposed: (1) super- or hyper-Eddington accretion for light seeds (e.g., Pacucci et al. 2015; Inayoshi & Haiman 2016; Ryu et al. 2016); (2) jump-starting from heavy seeds with a radiatively-efficient, thin-disk accretion model (e.g., Valiante et al. 2016; Pezzulli et al. 2017; Pacucci et al. 2017; Lupi et al. 2019); and (3) super-critical accretion through a radiatively-inefficient “slim disk” solution in which the radiative efficiency ϵ_r drops quickly as the accretion rate approaches super-Eddington (e.g., Sądowski 2009; Madau et al. 2014; Volonteri et al. 2015; Lupi et al. 2016; Pezzulli et al. 2016).

Indeed, numerous semi-analytical works have suggested that light seeds from Pop III stars can grow to $10^9 M_{\odot}$ by $z \sim 6$ with super- or hyper-Eddington accretion (e.g., Tanaka & Haiman 2009; Agarwal et al. 2013; Pezzulli et al. 2016; Ricarte & Natarajan 2018). To test these theories in detail, a number of groups have used hydrodynamical simulations to model the growth of SMBHs in the context of galaxy formation, taking into account gas dynamics, star formation, black hole accretion, and feedback processes. In par-

ticular, hydrodynamics simulations are essential for capturing the non-linear and intricate interplay between BH feedback and galaxy formation.

In an early study, Li et al. (2007) presented the first hydrodynamical simulation of the formation of $z \sim 6$ quasars, following the hierarchical mergers of protogalaxies of a $\sim 10^{13} M_{\odot}$ halo at $z \sim 6$, the most massive one in a $\sim 2.5 \text{ Gpc}^3$ volume, with $\sim 10^5 M_{\odot}$ BH seeds and a self-regulated BH growth model, as well as other important physical processes of star formation and feedback. They found that the seed BHs grow rapidly via efficient gas accretion facilitated by gas-rich mergers, producing a bright quasar at $z \sim 6.5$ with a $\sim 10^9 M_{\odot}$ SMBH. Subsequently, post processing the simulation with radiative transfer calculations and a supernova dust model, Li et al. (2008) found that the quasar reproduced a number of observational properties of many luminous quasars at $z \sim 6$.

Since then, BHs were included in direct cosmological simulations (Di Matteo et al. 2008), and more recently in a number of impressive large-scale simulations (*boxsize* $\sim 100 - 500 \text{ Mpc}$), such as Illustris (Vogelsberger et al. 2014b; Genel et al. 2014), EAGLE (Schaye et al. 2015; Crain et al. 2015), Horizon-AGN (Dubois et al. 2014), MassiveBlack (Khandai et al. 2015), BlueTides (Feng et al. 2016), Magneticum (Dolag et al. 2016), IllustrisTNG (Pillepich et al. 2018b; Springel et al. 2018; Weinberger et al. 2018; DeGraf & Sijacki 2020), and Simba (Davé et al. 2019). However, most of these simulations used similar BH recipes such as heavy seeds of $10^{4-6} M_{\odot}$ in $10^9 - 10^{10} M_{\odot}$ halos and Eddington-limited Bondi accretion, and due to the limitation in volume, or in resolution, or in the redshift range of the simulation, none of them produced $10^9 M_{\odot}$ SMBHs at $z > 6$ (the BlueTides Phase II was recently extended to $z \sim 7.4$ and it formed a single SMBH of $\sim 7 \times 10^8 M_{\odot}$ in the end, Tenneti et al. 2019). It is a common feature shared by the new generation of simulations that much stronger feedback is introduced, in particular a large mass loading in the outflow than models prior to 2014, to reproduce the stellar mass functions. It is interesting to ask whether the rare density peaks at high- z are then still able to produce luminous quasars. If not, what additional processes are required to reconcile discrepancies with observations? What do the quasar hosts look like? To address these questions, hydrodynamic simulations again prove to be a powerful tool.

It appears that high density peaks in the primeval initial conditions and high mass resolution are both required to study high- z quasars, which makes uniform cosmological simulations inefficient. To overcome the limitation set by the box size and resolution, zoom-in re-simulations of targeted regions, while retaining the large-scale tidal field using lower resolution particles, offer a viable route to model high- z quasars. Sijacki et al. (2009) performed a set of 6 zoom-in re-simulations of a massive halo with a mass $10^{13} M_{\odot}$ at $z = 6$ from the Millennium simulation with various resolutions, using conventional BH recipes ($10^{5-6} M_{\odot}$ seed in $10^9 - 10^{10} M_{\odot}$ halo) but also including BH gravitational recoil. They produced a $10^9 M_{\odot}$ SMBH at $z \sim 6$. Recently, several groups have performed various zoom-in simulations of massive halos using different codes, BH models and at various resolutions, and they achieved similar success in producing $\sim 10^9 M_{\odot}$ SMBHs at $z \gtrsim 6$ (e.g., Feng et al. 2014; Costa et al. 2014; Curtis & Sijacki 2016a; Smidt et al. 2018; Huang et al. 2020; Lupi et al. 2019).

Despite the impressive progress, most of the simulations have used similar models for BH seeds, accretion, and feedback (e.g., heavy seeds, Eddington-limited Bondi accretion, thin-disk with $\epsilon_r = 0.1$), with little investigation of other scenarios. It is therefore important to comprehensively study and compare various seed schemes, BH growth models and feedback processes. To this end, we

have performed a suite of 15 zoom-in cosmological simulations of a $10^{13} M_{\odot}$ halo at $z \sim 6$ similar to that of Li et al. (2007), with different BH seeds in the mass range of $10^1 - 10^6 M_{\odot}$, accretion modes from near-Eddington to super-, hyper- and unlimited-Eddington, and feedback models including both thin- and slim-disk accretion and radiation.

This paper is organized as follows. In Section 2, we describe the cosmological simulations and initial conditions in Section 2.1.2, the physical processes of star formation and feedback in Section 2.2, the BH seeds in Section 2.3, BH accretion in Section 2.4 and feedback in Section 2.5, and mergers in Section 2.6. In Section 3, we present the formation of the first quasars with our fiducial simulation, including the emergence of the first galaxies in Section 3.1, the growth history of a $10^9 M_{\odot}$ SMBH at $z \sim 6$ in Section 3.2, and the host galaxy properties in Section 3.3. In Section 4, we test different models with 15 zoom-in simulations, including BH seeds (Section 4.1), Eddington limits (Section 4.2), super-critical accretion and feedback (Section 4.3), and Bondi accretion variations and other parameters (Section 4.4), and we highlight the viable models for $z \sim 6$ quasars in Section 4.5. We discuss the limitations of our simulations and comparison with previous works in Section 5, and summarize our findings in Section 6.

2 METHODS

To study the formation of $z \gtrsim 6$ quasars with $10^9 M_{\odot}$ SMBHs, we have performed a suite of 15 zoom-in cosmological simulations of the same massive halo with different BH seeds of $10^1 - 10^6 M_{\odot}$, accretion modes from limited- to unlimited-Eddington, and feedback models including both thin- and slim-disk accretion and radiation. We describe the simulations, the physical processes, and the models in this Section.

2.1 The Cosmological Zoom-in Simulations

2.1.1 Hydrodynamics Code

The simulations were carried out with the Lagrangian particle code GIZMO (Hopkins 2015) with the implementation of physical processes by Zhu & Li (2016). GIZMO was developed to overcome problems encountered by smooth particle hydrodynamics (SPH) methods (Agertz et al. 2007; Bauer & Springel 2012; Zhu et al. 2015; Zhu & Li 2016). It solves the Riemann problem at the interface of two overlapping fluid elements, embodying the advantages of both SPH and grid-based methods. As a result, GIZMO captures the instabilities of fluid mixing well, and greatly reduces numerical noise and artificial viscosity.

As is the case with many cosmological simulations, sub-grid recipes are used to describe physical processes due to insufficient resolution to resolve individual stars or BHs (e.g., Vogelsberger et al. 2014b; Schaye et al. 2015; Khandai et al. 2015; Springel et al. 2018; Pillepich et al. 2018b; Davé et al. 2019). In Zhu & Li (2016), we have implemented in GIZMO a sub-grid recipe for star formation, multi-phase interstellar medium (ISM) and stellar feedback based on Springel & Hernquist (2003). Similarly, we have implemented a sub-grid recipe for BHs and related physical processes based on Springel et al. (2005a) and Di Matteo et al. (2005), in which BH accretion is calculated using a spherical Bondi model (Bondi & Hoyle 1944).

2.1.2 Initial Conditions

The target halo for the 15 zoom-in simulations is the most massive one within a $\sim \text{Gpc}^3$ volume, with a total mass of $1.16 \times 10^{13} M_{\odot}$ at $z = 6.1$. Note that while the halo is selected using the same technique as that in Li et al. (2007), the subsequent re-simulations are different in that the former performed a high-resolution hydrodynamical simulation of 6 major mergers from $z = 14.4$ to $z = 6$ extracted from the merger tree of the halo, but all the simulations here are full cosmological zoom-in simulations with hydrodynamics. This galaxy was shown to have a number of physical and panchromatic properties similar to some host galaxies of $z \sim 6$ quasars (Li et al. 2007, 2008).

To obtain the initial conditions for the zoom-in simulations, we first ran a dark matter - only parent simulation with 1024^3 particles in a $1 \text{ Gpc}/h$ box. We then selected the largest halo at $z = 6$ with the friend-of-friend (FOF) group-finding algorithm (Davis et al. 1985), and regenerated the initial conditions, which contain both dark matter and baryons, with a nested higher-resolution region of this halo using the multi-scale initial conditions code MUSIC (Hahn & Abel 2011). This high-resolution region has a size of $\sim 10 \text{ Mpc}/h$ (comoving) for the selected halo. Finally, the zoom-in simulations with the new initial conditions were run with a full list of comprehensive physical processes and models from $z = 99$ to 6.

2.1.3 Numerical Resolution and Cosmological Parameters

To determine the resolution for the zoom-in region, we had to consider a balance between the number of simulations and the cost of computations due to limited resources. In order to test the various models of BH seeding, accretion and feedback, we need at least 15 simulations, in addition to another set of 30 simulations to statistically study the properties of quasar hosts which will be presented in an upcoming paper. It is desired to have the same resolution for all these simulations for consistent comparisons, so we chose a reasonable resolution based on previous simulations (e.g., Sijacki et al. 2009; Feng et al. 2014; Costa et al. 2014; Curtis & Sijacki 2016a). Both (Sijacki et al. 2009) and (Feng et al. 2014) performed extensive resolution studies for their zoom-in simulations of early quasars, and found no significant effect of resolution on the final BH mass even when the resolution differed by a factor of 64, thanks to the numerically well behaved feedback model. Therefore, we chose a cost-effective resolution close to those of Sijacki et al. (2009) and Feng et al. (2014) with $m_{\text{gas}} = 6.5 \times 10^5 M_{\odot}/h$, $m_{\text{DM}} = 3.5 \times 10^6 M_{\odot}/h$, $\epsilon = 0.5 \text{ kpc}/h$, for particle mass resolution and gravitational softening length, respectively.

It is a significant challenge to include small BHs in cosmological simulations as we cannot achieve sufficient numerical resolution to resolve these objects due to limited computational resources. However, a large mass ratio between particles may cause two-body heating and other numerical problems. To alleviate these potential numerical artifacts, we adopted a numerical technique used by Springel & Hernquist (2003) to treat star formation, in which a fraction of a gas particle becomes a new star, to treat BH seeds of $10 - 100 M_{\odot}$ from remnants of Pop III stars in our simulations. The newly formed BH is treated as a fraction of the parent Pop III star particle from which the BH formed, while the parent star particle becomes a “ghost particle” associated with the new BH. The “ghost particle” interacts with other particles only via gravity; the BH particle has the same dynamics as its “ghost” while maintaining its own mass and accretion activity. This technique reduces two-body relaxation as the star particles have comparable mass as other particles,

and it enables small BHs to robustly evolve and grow consistent with other massive BHs.

The simulations were run with a set of cosmological parameters consistent with the WMPA 1- and 5-year results (Spergel et al. 2003; Komatsu et al. 2009): $\Omega_M = 0.25$, $\Omega_b = 0.04$, $\Omega_\Lambda = 0.75$, $h = 0.73$ and $\sigma_8 = 0.9$. We have also re-run the fiducial simulation with the cosmological parameters from Planck Collaboration et al. (2016): $\Omega_M = 0.308$, $\Omega_b = 0.048$, $\Omega_\Lambda = 0.692$, $h = 0.678$ and $\sigma_8 = 0.82$, and found no significant differences between the two simulations, as shown in Section 4.

2.1.4 List of Simulations

As listed in Table 1, the 15 zoom-in simulations of the same halo aim to test various models and parameters, with different BH seeds of $M_{\text{seed}} = 10^1 - 10^6 M_\odot/h$, Eddington limits of $\max(\lambda_{\text{Edd}}) = 1 - 10^4$, and feedback from both constant- ϵ_r radiatively-efficient accretion and varying- ϵ_r from super-critical accretion models, as well as variations in Bondi accretion and cosmological parameters. Note in the simulations, we use units with the dimensionless Hubble parameter h such as M_\odot/h and kpc/h , but we present the results with h -less units for direct comparison with observations. The physical processes will be described in detail in the next sections.

2.2 The Physics of Star Formation and Feedback

2.2.1 Star Formation and Multi-phase ISM

We use the sub-grid multi-phase interstellar medium model of Springel & Hernquist (2003) for star formation and thermal feedback. In this model, gas consists of cold and hot phases, so the total gas density ρ is the sum of ρ_c and ρ_h , $\rho = \rho_h + \rho_c$. In star-forming gas, the evolution of the cold/hot phases is governed by star formation, supernovae explosions, and heating and cooling. At high density ($\sim 10^5 \rho_{\text{th}}$), this two-phase model returns a close-to-unity mass fraction of cold phase gas fueling rapid star formation.

For each star-forming gas particle, surrounding gas is pressurized according to the multi-phase model that balances the evaporation of cold gas and cooling of hot gas that is explicitly solved in coupled equations. This approach naturally gives additional pressure support against self-gravity. Moreover, Springel & Hernquist (2003) showed that this method has good numerical convergence properties. We adopt a Chabrier initial mass function (IMF) with the stellar mass ranging between $[0.1, 100] M_\odot$. Stars more massive than $8 M_\odot$ explode as Type II supernovae and return the mass and metals into the surrounding ISM. The number density threshold for star formation is 0.13 cm^{-3} , which is commonly used in such cosmological simulations.

2.2.2 Metal Enrichment and Cooling

Radiative cooling of optically thin gas is modeled using the cooling table from Smith et al. (2017). The cooling curves are generated with CLOUDY for gas exposed to a redshift-dependent UV background from Faucher-Giguère et al. (2010). We adopt an exact time integration scheme introduced by Townsend (2009) to update the thermal energy due to radiative cooling (Zhu et al. 2017).

To model stellar evolution and chemical enrichment, we treat each star particle as a simple stellar population with an initial total mass of $10^6 M_\odot$, and a metallicity in the range of $Z = [0.0004, 0.004, 0.008, 0.02, 0.05]$, adopting a Chabrier initial mass function. Then each stellar population is evolved with

stellar population synthesis (SPS) code STARBURST99 (Leitherer et al. 1999, 2011) with Padova models (including the contribution of AGB stars) to produce tables of enrichment from both Type II SNe and AGB stars. At each time step, we tabulate the returned mass and chemical enrichment from active star particles by linear interpolation on a 2D grid of stellar age and metallicity.

2.2.3 Feedback from Supernovae

Even with the sub-grid multi-phase ISM model of Springel & Hernquist (2003), galactic outflows are difficult to generate since most of the thermal energy from SNe is in the form of the effective pressure. A model of “energy-driven” winds (Vogelsberger et al. 2013) is a phenomenological approach to address the observed low star formation efficiency in low mass halos by launching gas into a galactic wind. We implement this model into our codes, assuming 70% of the supernovae energy is available to launch the wind in two polar directions. Once a particle is flagged as a wind particle, we temporarily decouple it from hydrodynamics as in Springel & Hernquist (2003) and Vogelsberger et al. (2013) to allow the wind particles to travel up to a certain distance away from star-forming regions, but when the gas density around the wind particle is a factor of 0.1 of the density threshold for star formation, the wind particles are re-coupled hydrodynamically. This model successfully produces a realistic L^* galaxy with a well-defined stellar disk like the Milky Way, as demonstrated by Zhu & Li (2016).

2.3 The Black Hole Seeds

Currently, there are three competing theories for the seeds of SMBHs which grow quickly into bright quasars. The mass of the BH seeds varies from $10-100 M_\odot$ for stellar BHs from the first stars to $10^5 M_\odot$ for the direct collapse of pre-galactic gas clouds. Unfortunately, our understanding of the first stars and the processes of direct collapse are both limited due to the complexity of the physical mechanisms involved. Therefore, the seed BH mass is treated as a free parameter in current cosmological hydrodynamic simulations.

2.3.1 Light BH seeds

The first stars that formed out of primordial gas between $z = 20-30$ in $\sim 10^6 M_\odot$ halos provide a natural channel to form the first BHs after their brief lifetimes (see a recent review by Haemmerlé et al. 2020). The IMF of Pop III stars is still poorly constrained due to the interplay between gas cooling, turbulence, radiation, the evolution of accretion disks, and possibly magnetic fields (e.g., Stacy et al. 2016; Hirano & Bromm 2017; Chon & Hosokawa 2019; Fukushima et al. 2020; Sugimura et al. 2020).

It has been suggested that the BHs from Pop III stars have a mass in the range of $10 - 100 M_\odot$ (e.g., Volonteri & Bellovary 2012; Madau et al. 2014; Latif & Ferrara 2016; Valiante et al. 2016; Becerra et al. 2018; Woods et al. 2019; Inayoshi et al. 2020). We implemented a simplified model of BH seeds from Pop III stars. Since we directly follow the chemical enrichment from stellar evolution, we are able to track the gas metallicity throughout the simulation. So we use the stellar metallicity as a criterion to select BH seeds. When a star particle metallicity of Z is below a critical value of $10^{-4} Z_\odot$, we convert this particle into a BH particle 2 Myr after the star is born. The critical metallicity is similar to the value $10^{-3.8} Z_\odot$ used in Valiante et al. (2016); Pezzulli et al. (2016). We

Table 1. Summary of the 15 cosmological zoom-in simulations and model parameters.

Simulation	Model Description	M_{seed} [M_{\odot}/h]	Seeding Scheme	Accretion & Feedback	ϵ_r	$\max(\lambda_{\text{edd}})$	M_{BH} [M_{\odot}/h]
Seed Models							
S1	Light Seed	10^1	PopIII	Super-critical, $a = 0$	Eq. (8)	10^4	7.3×10^4
S2	Light Seed	10^2	PopIII	Super-critical, $a = 0$	Eq. (8)	10^4	2.5×10^6
S3	Intermediate Seed	10^3	Halo	Thin disk	0.1	1	5.1×10^6
S4	Intermediate Seed	10^4	Halo	Thin disk	0.1	1	2.4×10^8
S5-REF	Heavy Seed, Fiducial	10^5	Halo	Thin disk	0.1	1	2.7×10^9
S6	Heavy Seed	10^6	Halo	Thin disk	0.1	1	6.8×10^9
Eddington Limits							
S5-EL1	Super-Eddington	10^5	Halo	Thin disk	0.1	2	7.6×10^8
S5-EL2	Super-Eddington	10^5	Halo	Thin disk	0.1	5	1.8×10^8
S5-EL3	Hyper-Eddington	10^5	Halo	Thin disk	0.1	10^4	7.2×10^6
Feedback Models							
S5-FB1	Slim disk, no spin	10^5	Halo	Super-critical, $a = 0$	Eq. (8)	10^4	5.8×10^9
S5-FB2	Slim disk, maximal spin	10^5	Halo	Super-critical, $a = 0.99$	Eq. (8)	10^4	4.0×10^8
S5-FB3	High radiative feedback	10^5	Halo	Thin disk	0.2	1	2.7×10^7
Bondi Accretion Variations							
S5-BA1	Bondi constant α	10^5	Halo	Thin disk, $\alpha = 100$	0.1	1	2.2×10^9
S5-BA2	Bondi power-law α	10^5	Halo	Thin disk, $\alpha = (\rho/\rho_{\text{th}})^2$	0.1	1	6.9×10^8
Cosmological Parameters							
S5-CP	Planck parameters	10^5	Halo	Thin disk	0.1	1	2.6×10^9

Notes: (1) Simulation name. (2) Model description. (3) Black hole seed mass. (4) Black hole seeding scheme. Light seeds come from Pop III stars with metallicity $Z \leq 10^{-4}$, while intermediate and heavy seeds are planted in the host halo when its virial mass $M_{200} = 10^{10} M_{\odot}/h$ at redshift $z = 18.8$. (5) Accretion and feedback model. The accretion rate is calculated using Eq. (5), while the feedback is described by the radiative efficiency ϵ_r . For the thin disk model $\epsilon_r = 0.1$, while for the slim disk model ϵ_r depends on the BH mass, accretion rate and spin, as calculated using Eq. (8). (6) Radiative efficiency of BH accretion. (7) Maximum Eddington limit. The hyper-Eddington model is set with a high number $\max(\lambda_{\text{edd}}) = 10^4$ in the simulation. (8) The final black hole mass in the simulations at redshift $z = 6.16$. Note S5-REF is the fiducial simulation for comparison reference in this study.

test two seed masses of $M_{\text{seed}} = 10$ and $100 M_{\odot}/h$ for this model with simulations.

It is obvious that the resolution of our simulations cannot resolve these small BHs, and that the mass ratio between other particles and the BHs is very large, which could cause two-body relaxation and other numerical artifacts. As described in Section 2, in order to alleviate the problems, we have adopted a numerical technique to treat the BH as a fraction of the Pop III star particle from which it was born, similar to that used by Springel & Hernquist (2003) to treat star formation in which a fraction of the gas particle becomes a new star, while the parent star particle becomes a “ghost” attached to the BH. Since the “ghost particles” have comparable mass as the gas and dark matter particles, this technique reduces two-body heating and allows the BH particle to have the same dynamics as its parent star particle while maintaining its own mass and accretion activity. As we will see in Section 4.1, this treatment enables the small BHs to obtain consistent growth paths as their massive counterparts.

2.3.2 Intermediate BH Seeds

BH seeds with mass $\sim 10^3 M_{\odot}$ may result from collisional dynamics within dense star clusters in the early Universe (Portegies Zwart & McMillan 2000; Freitag et al. 2006a,b). Using N-body simulations, Portegies Zwart & McMillan (2002) demonstrate that in a very

dense star cluster a massive star of $10^3 M_{\odot}$ could form due to stellar collisions. Recently, Katz et al. (2015) and Yajima & Khochfar (2016) have studied this channel and found a very massive star of $\sim 10^3 M_{\odot}$ can appear at redshifts as high as $z \sim 20$. Subsequently, the very massive stars can form BHs without going through a supernova stage. Alternatively, Woods et al. (2017, 2019) argued that $\sim 10^3 M_{\odot}$ can also form from super-massive stars. For this model, we test two seed masses of $M_{\text{seed}} = 10^3$ and $10^4 M_{\odot}/h$ with simulations.

Since the formation conditions of the intermediate BHs are uncertain, it is difficult to determine when and where they form, so for direct comparison with the heavy seeds, we use the same scheme as the latter to plant the seeds of 10^3 and $10^4 M_{\odot}/h$ in halos with mass $M_{200} = 10^{10} M_{\odot}/h$.

2.3.3 Heavy BH Seeds

BH seeds could also form in the isothermal collapse of gas clouds in atomic-cooling halos ($T_{\text{vir}} \geq 10^4$ K) (Rees 1978; Bromm & Loeb 2003; Begelman et al. 2006; Mayer et al. 2010; Johnson et al. 2011; Inayoshi et al. 2015; Becerra et al. 2015; Regan et al. 2017; Wise et al. 2019). The physical processes, as depicted by Begelman et al. (2006), show that the high density gas may quickly develop runaway global gravitational instabilities in the form of “bars within bars”, efficiently transferring angular momentum outwards, to form a dense gas core. Then, a central black hole can form in this dense

core due to catastrophic cooling via thermal neutrinos if very high core temperature is achieved. The formation of direct collapse seeds depends sensitively on the location of the cooling halo, where H_2 formation and fragmentation is supposed to be suppressed by the UV radiation from nearby Pop III and Pop II stars. The early chemical enrichment and the intensity of H_2 dissociating UV background are among the top uncertainties in modeling direct collapse. At redshift $z = 15 - 18$, a seed BH of $10^5 M_\odot$ could form in $10^7 - 10^8 M_\odot$ halos based on the most recent studies (Valiante et al. 2017). Alternatively, other routes have been proposed to form massive BHs via merger-driven direct collapse (e.g., Mayer et al. 2010; Mayer & Bonoli 2019).

Our simulation does not include the necessary resolution and physical process to model direct collapse. Instead, we follow the method used in previous studies (e.g., Li et al. 2007; Di Matteo et al. 2008; Vogelsberger et al. 2014b; Schaye et al. 2015; Khandai et al. 2015; Springel et al. 2018; Pillepich et al. 2018b) to place a massive BH seed at the center of halos with masses above a threshold $M_{200} = 10^{10} M_\odot/h$, identified by frequently running the FOF algorithm on the fly. In this study, we test two seed masses of $M_{\text{seed}} = 10^5$ and $10^6 M_\odot/h$, respectively, for this model.

2.4 Black Hole Accretion

One of the most important channels of BH mass growth is the accretion of gas. Bondi & Hoyle (1944) described the accretion rate \dot{M}_{BH} around a central mass M_{BH} embedded in isothermal gas without net angular momentum as:

$$\dot{M}_{\text{BH}} = \frac{4\pi G^2 M_{\text{BH}}^2 \rho}{(c_s^2 + v^2)^{3/2}}, \quad (2)$$

where ρ , c_s and v are the gas density, sound speed and relative velocity between gas and central mass M_{BH} , respectively.

However, it is currently not feasible to use the above expression directly in the cosmological simulations, which do not resolve the physical scales of black accretion (but see recent work by Curtis & Sijacki 2015 and Hopkins et al. 2016). Instead, most of the simulations adopt a sub-grid description that is often optimized towards more efficient accretion than that based on the simple Bondi-Hoyle accretion rate. In this study, we compare the following models used in some recent simulations.

2.4.1 Constant Boost Factor α of Bondi Accretion

This model was first proposed by Springel et al. (2005a) to adjust the effects of numerical resolution on the accretion rate with a constant boost factor α :

$$\dot{M}_{\text{BH}} = \frac{\alpha 4\pi G^2 M_{\text{BH}}^2 \rho}{(c_s^2 + v^2)^{3/2}} \quad (3)$$

The numerical value α is set to 100 (Sijacki et al. 2009), which is calibrated with local scaling relations using galaxy merger simulations (Springel et al. 2005a; Di Matteo et al. 2005). This was the approach employed in the original Illustris simulations (Vogelsberger et al. 2014c). In the IllustrisTNG Project, however, no boost factor was applied to the estimated accretion rate.

2.4.2 Power-law Boost Factor α of Bondi Accretion

Booth & Schaye (2009) argued that the above model tends to overestimate the accretion rate around a BH when the physical scale

of gas is well-resolved, which could occur for low-density high-temperature non-star forming gas. Instead, they propose a density-dependent α model:

$$\alpha = \begin{cases} 1, & \rho < \rho_{\text{th}} \\ \left(\frac{\rho}{\rho_{\text{th}}}\right)^\beta, & \rho \geq \rho_{\text{th}} \end{cases} \quad (4)$$

This model uses a power-law index β to capture the unresolved ISM physics while returns to the nominal Bondi-Hoyle rate for non-star forming gas. This model is also adopted in the RAMSES simulations (Dubois et al. 2012).

2.4.3 Chaotic Gas Accretion From Cold Clouds

The switch between non-star forming and star-forming gas is certainly not unique. For example, Pelupessy et al. (2007) suggested a model based on a two-phase ISM as an alternative to eliminate the α factor. Instead of using ρ and u , the accretion rate of star-forming gas is split into the contribution from both cold and hot phases. Since the accretion rate scales as $\rho/(c_s^2 + v^2)^{3/2}$, the accretion mostly comes from the cold gas phase:

$$\dot{M}_{\text{BH}} = \frac{x 4\pi G^2 M_{\text{BH}}^2 \rho}{(c_{s,\text{cold}}^2 + v^2)^{3/2}} + \frac{(1-x) 4\pi G^2 M_{\text{BH}}^2 \rho}{(c_{s,\text{hot}}^2 + v^2)^{3/2}} \quad (5)$$

where the mass fractions of cold gas $c_{s,\text{cold}}$ and hot gas $c_{s,\text{hot}}$ around the BH are obtained using the cold – hot ISM break down in Springel & Hernquist (2003).

Physically, this model aims to capture the large amount of molecular clouds around BHs, as recently been observed by Tremblay et al. (2016). This model resembles the chaotic accretion in Gaspari et al. (2013, 2015) and it will be our fiducial choice for the gas accretion rate estimate.

This Bondi-based accretion model is different from that in the Simba simulation (Davé et al. 2019), in which the BH accretion rate estimator scales linearly with the gas inflow rate via gravitational torque for the cold gas, while for the hot gas it uses the Bondi accretion. The Simba accretion model would produce an invariant $M_{\text{BH}} - M_\star$ correlation across time, because both BHAR and SFR scale with the gas inflow rate. However, observations suggest that the $z \sim 6$ quasars do not seem to follow the local $M_{\text{BH}} - M_\star$ correlation (e.g., Wang et al. 2013; Venemans et al. 2018; Pensabene et al. 2020).

In this study, we test the chaotic cold accretion variations in the Bondi estimate of the BH accretion rate. We use the Eddington ratio λ_{Edd} to describe the accretion mode, which is the ratio of the BH accretion rate to the Eddington rate:

$$\lambda_{\text{Edd}} = \frac{\dot{M}_{\text{BH}}}{\dot{M}_{\text{edd}}} \quad (6)$$

where the Eddington accretion rate \dot{M}_{edd} ¹ is calculated as:

$$\dot{M}_{\text{edd}} = \frac{4\pi G M_{\text{BH}} m_p}{\epsilon_r \sigma_T c} = \frac{L_{\text{Edd}}}{c^2 \epsilon_r}, \quad (7)$$

where m_p is the proton mass, ϵ_r is the radiative efficiency and σ_T is the Thompson cross-section.

We define three modes of accretion based on past convention: near-Eddington for $0.6 \leq \lambda_{\text{Edd}} \leq 1$, super-Eddington for

¹ In the case of super-critical accretion, we use the definition $\dot{M}_{\text{edd}} = 16 L_{\text{Edd}}/c^2$ as in Madau et al. (2014).

$1 < \lambda_{\text{Edd}} \leq 10$, and hyper-Eddington for $\lambda_{\text{Edd}} > 10$. In the simulations, we use a free parameter $\max(\lambda_{\text{Edd}})$ to limit the maximum accretion rate in order to investigate the effects of these different modes on the BH growth.

2.5 Black Hole Feedback

As suggested by [Springel et al. \(2005a\)](#), feedback from BHs generally falls in two modes depending on the accretion rate: the quasar and radio modes for high and low accretion rates, respectively. Since we focus on the quasar phase of early SMBHs in this study, we only consider “quasar feedback”, which couples the radiation from BH accretion to surrounding gas in the form of thermal energy with a fixed fraction of $\epsilon_r \epsilon_f$, where ϵ_r is the radiative efficiency, and ϵ_f is the efficiency of converting radiation into thermal energy, which is typically fixed at 5% as suggested by [Di Matteo et al. \(2005\)](#).

The thermal energy is then distributed isotropically to the surrounding gas. There are some subtleties related to the coupling of thermal feedback energy in the two-phase ISM model. For non-star forming gas, the thermal injection from BHs is a simple additional term to the gas thermal energy, but for star-forming gas, the thermal energy from BHs is coupled to that from SNe and distributed over a characteristic decay timescale, as described in [Springel et al. \(2005a\)](#). Note even within this simple model, large theoretical uncertainties are present due to our current understanding of BH accretion disks (e.g., see reviews by [Abramowicz & Fragile 2013](#) and [Haemmerlé et al. 2020](#)).

For this study, we consider two feedback mechanisms: radiatively-efficient thin-disks with constant ϵ_r , and super-critical slim-disks with varying ϵ_r depending on the BH mass, accretion and spin, as described below.

2.5.1 Thin-disk Radiative Accretion with Constant ϵ_r

Our fiducial choice of $\epsilon_r = 0.1$ is the same value used in [Springel et al. \(2005a\)](#), which corresponds to the radiatively-efficient thin disk model of [Shakura & Sunyaev \(1973\)](#). This model assumes local thermal equilibrium and is such that the heat generated by viscosity is radiated away immediately. This model is widely adopted in cosmological simulations. The numerical value of the radiative efficiency ϵ_r ranges from 0.1 ([Springel et al. 2005a](#); [Di Matteo et al. 2005](#)), to 0.15 ([Booth & Schaye 2009](#)), and to 0.2 ([Vogelsberger et al. 2013](#)). Similar to the seed mass, ϵ_r is another important parameter in cosmological simulations with BHs.

As listed in Table 1, we also test this model with $\epsilon_r = 0.2$ to investigate the effects of radiation on BH growth.

2.5.2 Slim-disk Super-critical Accretion with Variable ϵ_r

Once the accretion luminosity is high ($L \geq L_{\text{Edd}}$), the radiative efficiency drops due to the fact the heat generated by viscosity is insufficiently radiated away and the radial velocity within the disk cannot be neglected. Advection within the accretion disks dominant. As a result, a substantial amount of heat is transported inwards by gas advection thus reducing the overall radiative efficiencies. [Abramowicz et al. \(1988\)](#) first proposed a slim-disk model that describes a super-critical radiatively inefficient accretion flow. Recently [Madau et al. \(2014\)](#) have (also used by [Lupi et al. 2016](#)) fitted the radiative efficiency as a function of high accretion rate \dot{M}_{BH} and black hole

spin parameter a according to the solutions constructed by [Sądowski \(2009\)](#) with the following functions:

$$\epsilon_r = rA(a) \left[\frac{0.985}{r+B(a)} + \frac{0.015}{r+C(a)} \right], \quad (8)$$

$$r = \frac{L_{\text{Edd}}}{\dot{M}_{\text{BH}} c^2} = \frac{1}{\dot{M}_{\text{BH}}} \frac{4\pi G M_{\text{BH}} \mu_e m_p c}{c^2 \sigma_T}.$$

where the functions $A(a)$, $B(a)$ and $C(a)$ depend on BH spin a :

$$\begin{aligned} A(a) &= (0.9663 - 0.9292 a)^{-0.5639}, \\ B(a) &= (4.6270 - 4.4450 a)^{-0.5524}, \\ C(a) &= (827.30 - 718.10 a)^{-0.5639}. \end{aligned} \quad (9)$$

In this model, the radiative efficiency ϵ_r quickly drops from ~ 0.05 to ~ 0.01 for non-spinning BHs accreting at super-Eddington rates. For BHs with a maximum spin of $a \sim 1$, ϵ_r is considerably higher. Despite the super-Eddington rate of BH mass accretion, because of low radiative efficiency the resultant luminosity may appear moderately super-Eddington with $\max(\lambda_{\text{Edd}}) \sim 3$ ([Madau et al. 2014](#)). Recently, [Sądowski et al. \(2016\)](#) and [Narayan et al. \(2017\)](#) have found that, while the radiative efficiency for the slim-disk accretion is low, large mechanical power in the form of jets and outflows can be released.

A proper treatment of super-critical accretion thus requires more inputs from small-scale simulations of accretion flows around BHs.

For this study, we test the super-critical accretion model for both light BH seeds of 10, 100 M_{\odot}/h from Pop III stars and heavy seeds of $10^5 M_{\odot}/h$, as listed in Table 1. Although it is possible to calculate the spin of a BH in the simulation by tracking the angular momentum of all the gas particles accreted by the BH, it is time consuming to do so on-the-fly for all the BHs in the simulations, so in practice we use two spins $a = 0$ and $a = 0.99$ to bracket the spin range to investigate the effects of spin on BH growth.

2.6 Black Hole Mergers

In addition to gas accretion, BHs can grow through binary mergers. In our simulations, BH binary mergers happen whenever two BHs are within the smoothing radius of either BH and the relative velocity between the two BHs is below the circular velocity of the BH pair ([Booth & Schaye 2009](#)).

During the merger of two BHs, a large velocity kick might be expected for the remnant because of gravitational recoil ([Bekenstein 1973](#); [Volonteri & Rees 2006](#); [Blecha & Loeb 2008](#)). The recoil velocity, which depends upon the mass ratio of the BH binary and the spins of each BH, can temporarily kick the BH from the center of the galaxy and delay its mass accretion as shown by [Blecha et al. \(2011\)](#). Gravitational recoil has been included in some simulations (e.g., [Sijacki et al. 2009](#); [Kelley et al. 2017](#)). In particular, [Kelley et al. \(2017\)](#) presented a comprehensive modeling of the recoiling BH including processes such as dynamical friction, stellar loss-cone scattering, and gas drag. In our simulations, we do not consider BH recoil in the modeling, because as demonstrated in [Li et al. \(2007\)](#), the escape velocity of this massive host halo we selected is large enough even for the most extreme recoil velocities, and our main targets are the most massive BHs in the galaxies, which are usually located in the deepest potential well of the hosts.

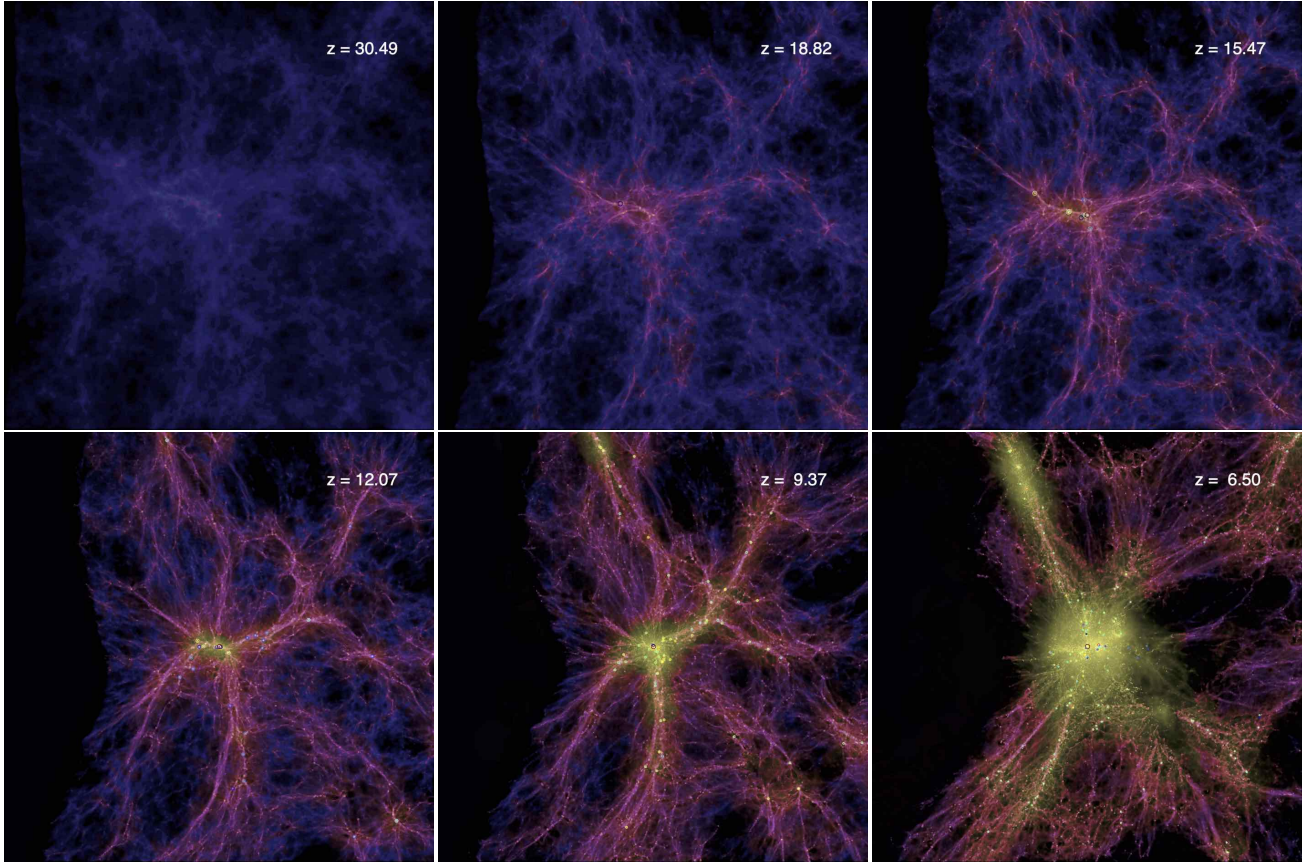


Figure 1. The emergence of the first galaxies and BHs and their evolution from $z \sim 30$ to $z \sim 6.5$ in the fiducial S5-REF simulation. The images are the projected gas density, color-coded by temperature: blue represents cold, while yellow represents hot gas heated and ionized by feedback from supernovae and accreting BHs. The colored circles indicate locations of the BHs. The zoom-in region is ~ 10 comoving Mpc centered on a galaxy halo of $\sim 1.16 \times 10^{13} M_{\odot}$ at $z = 6.1$, the most massive one in a Gpc^3 volume.

3 FORMATION OF THE FIRST QUASARS

In this Section, we present the formation and evolution of the first galaxies and black holes from the S5-REF simulation, which covers the region of the largest halo at $z \sim 6$ in a $(1 \text{ Gpc}/h)^3$ volume. As listed in Table 1, the S5-REF simulation is our fiducial model with a heavy seed of $10^5 M_{\odot}/h$ BHs are planted in a halo when its mass reaches $10^{10} M_{\odot}/h$, and the BH grows with the canonical Eddington-limited, thin-disk chaotic accretion with a constant $\epsilon_r = 0.1$. It also includes all the physics of a multi-phase ISM, star formation, and feedback processes, as described in Section 2.

3.1 Emergence of the First Galaxies

The S5-REF simulation is a highly overdense region where the first galaxies are expected to form. Figure 1 shows the cosmic web of this region and its evolution from $z = 30.45$ to $z = 6.16$. The filamentary structure formed under gravity from perturbations, and the first mini halos collapsed in the dense intersections of the filaments and continued to grow through accretion and mergers with other mini halos. When these atomic-cooling halos reach mass $\gtrsim 10^6 M_{\odot}$ and temperature $T_{\text{vir}} \gtrsim 10^4 \text{ K}$ at $z \sim 30$, Pop III stars form in the metal-free gas. These first stars evolved rapidly, and the feedback, metal enrichment and remnants from the stars shaped the subsequent formation of galaxies. In the simulation, the first BH seed emerged in the largest halo at $z \sim 18.8$ when it reached $10^{10} M_{\odot}/h$.

The largest halo has undergone more than two dozen major mergers from $z \sim 24$ to $z \sim 6$ when it assembled a mass of $6.86 \times 10^{12} M_{\odot}/h$. These gas-rich galaxy mergers provide an abundant gas supply and compress the gas to high density in the central galaxy. Figure 2 shows the gas distribution of the central galaxy at $z = 7.5$ from the simulation. A large amount of cold gas is continuously channelled into the central galaxy from the filaments and frequent mergers. In the central region of the galaxy, a disk-like gas distribution with a bar-like structure and spiral arms are present. Such a structure is highly unstable and it facilitates efficient angular momentum transport of the gas to fuel a vigorous circumnuclear starburst and rapid black hole accretion in the center.

Figure 3 shows the distribution of gas and stars of a merger sequence from $z = 9.13$ to $z = 6.1$. During the merger event, a nuclear gas disk is formed in the central region. The axis of the nuclear gas disk is misaligned with the outer gas distribution, as can be seen between $z = 8.63$ and $z = 8.37$. This behavior is similar to the nuclear disk formed in the merger simulations by Barnes & Hernquist (1996), who showed that the remnant of the nuclear disk becomes part of the central stellar bar later on.

The tidal torques are an efficient means to transfer gas angular momentum (Hopkins & Quataert 2010), which is manifested in the forms of density waves, in particular in cases involving $m = 1, 2$ (number of spiral arms). The strong features of spiral arms, bars and misaligned gas planes in multiple snapshots in Figure 3 indicate

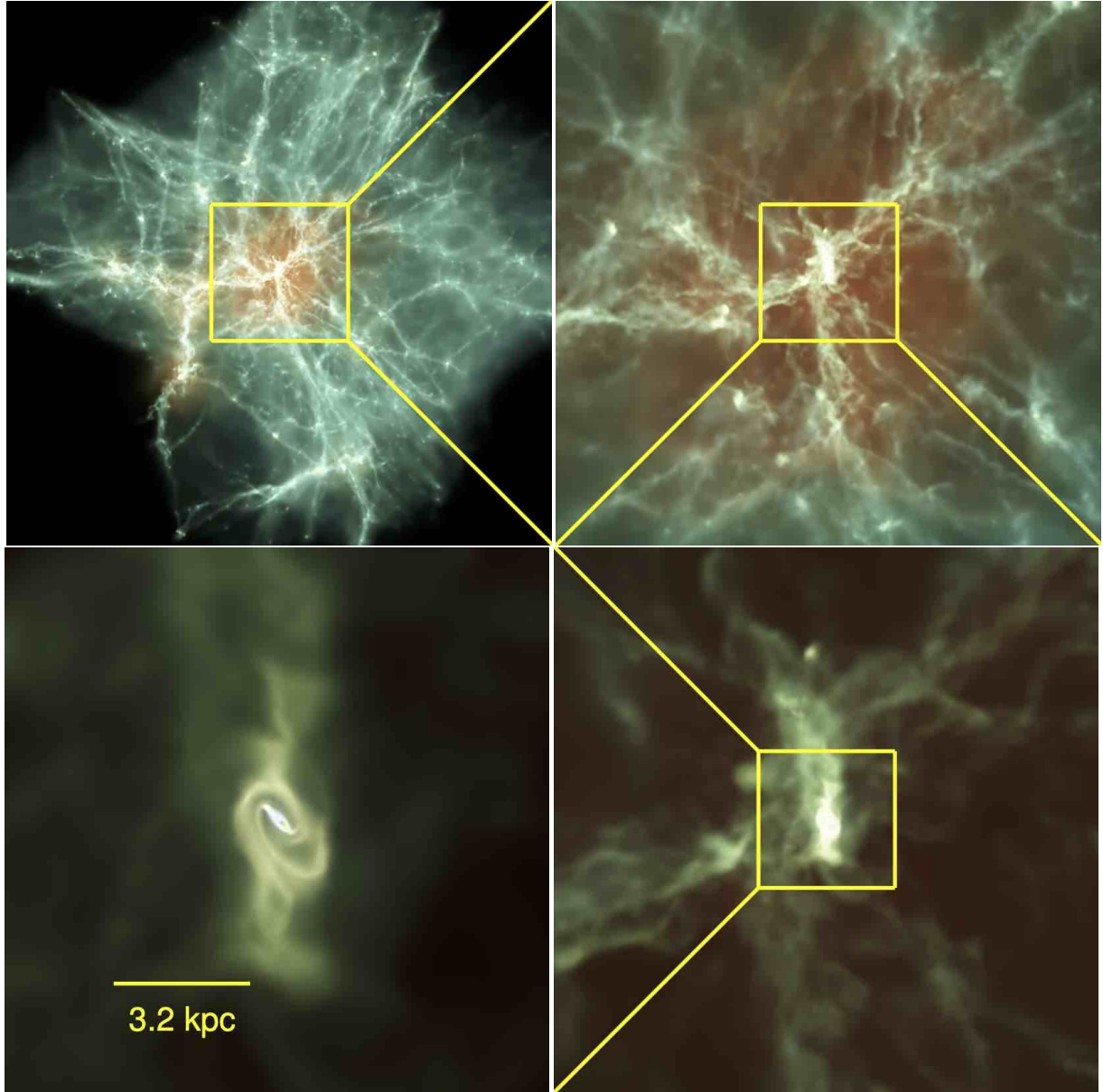


Figure 2. The gas distribution of the central galaxy at $z = 7.5$ from the S5-REF simulation. The images are the projected gas density at different scales. In the central 3 kpc region, the gas forms a disk with spiral arms connected to the central bar-like structure.

that a strong gas inflow induced by torques is taking place at these redshifts.

In order to quantify the effects of tidal torques on angular momentum transport and gas inflow, we compare three timescales: angular momentum transport timescale t_{ang} , local dynamical timescale t_{dyn} , and gas depletion timescale t_{dep} .

The angular momentum transport timescale t_{ang} is defined as the ratio between the angular momentum $\mathbf{L} = \mathbf{r} \times \mathbf{v}$ and tidal torques $\boldsymbol{\tau} = \mathbf{r} \times \mathbf{F}/m$:

$$t_{\text{ang}} = \frac{\tau}{\dot{\mathbf{L}}} = \frac{\mathbf{r} \times \mathbf{F}/m}{\mathbf{r} \times \mathbf{v}}. \quad (10)$$

where \mathbf{r} , m , $\mathbf{v}(\mathbf{r})$ and $\mathbf{F}(\mathbf{r})$ are the radius, mass, velocity of the gas and force on the gas at the location, respectively.

The local dynamical timescale t_{dyn} is defined as:

$$t_{\text{dyn}} = \frac{2\pi r}{v_{\text{cir}}(r)}. \quad (11)$$

where $v_{\text{cir}}(r)$ is the circular velocity at the radius r .

The gas depletion timescale t_{dep} by star formation is defined as:

$$t_{\text{dep}} = M_{\text{gas}}/\text{SFR}, \quad (12)$$

where M_{gas} and SFR are the total mass of star-forming gas and total star formation rate at each r , respectively.

The difference between the timescale for angular momentum exchange and the dynamical timescale is key to understanding the origin of the angular momentum transport. [Tohline et al. \(1982\)](#) showed that gravitational torques cause misaligned gas to settle into a preferred plane and the timescale of this settling process

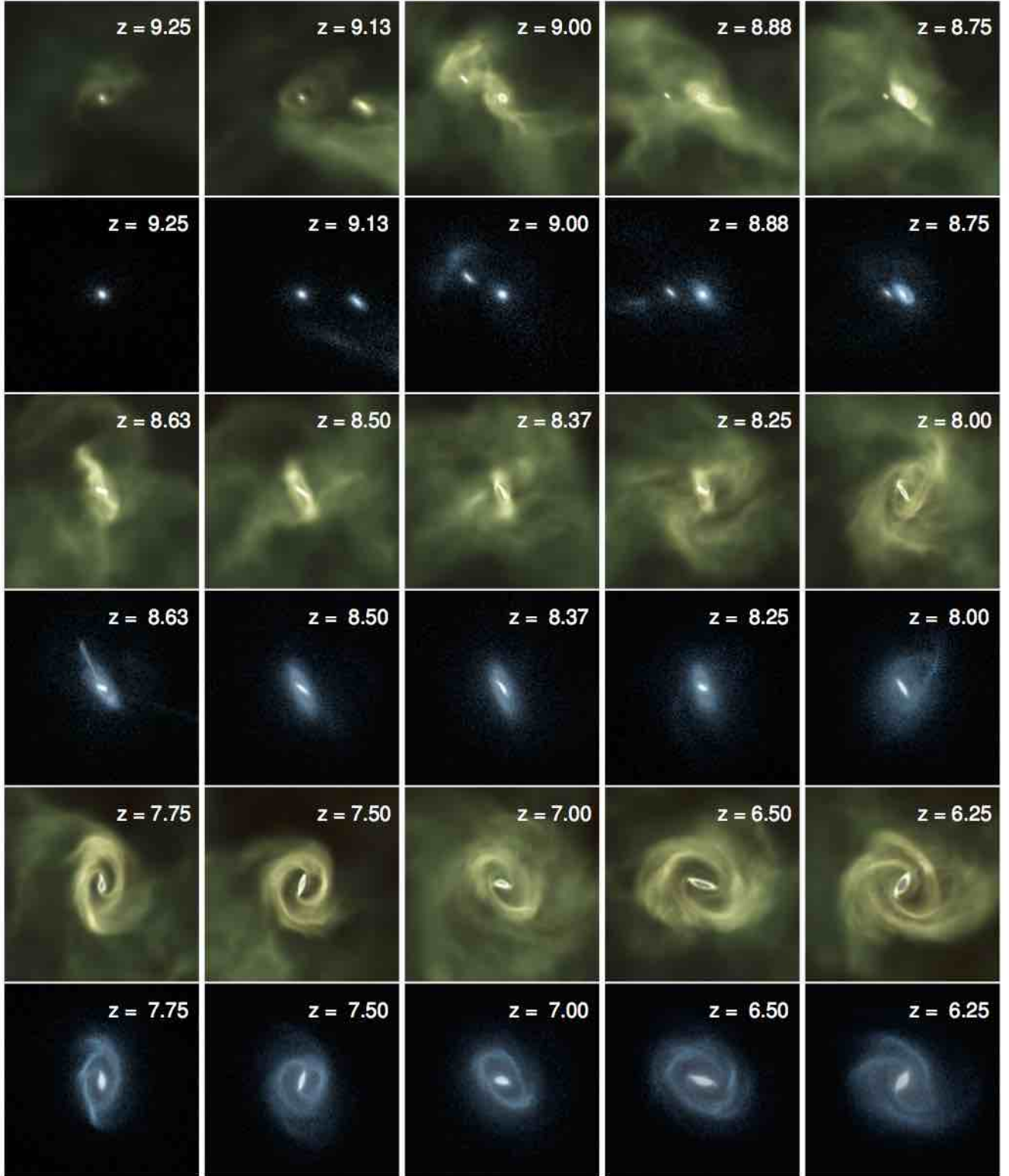


Figure 3. A time sequence of the merger event between $z = 9.13$ and $z = 6.1$ from the S5-REF simulation. The images are the projected gas density at different redshifts and corresponding projected stellar density. The size of each panel is 10 kpc in physical coordinates. The stellar map is color-coded using stellar photometry from Starburst99 (Leitherer et al. 1999, 2011) based on the metallicity and stellar age such that old stellar population appears in red while the young one is in blue.

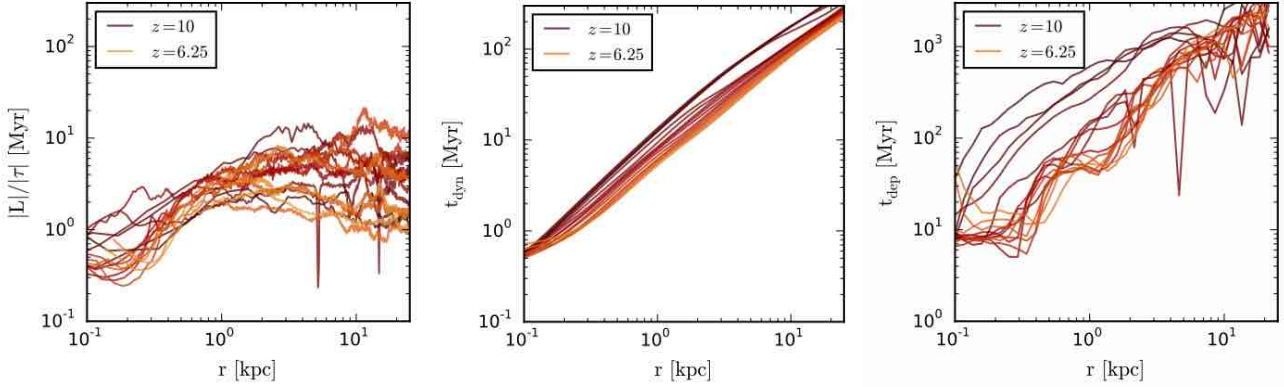


Figure 4. A comparison of the angular momentum transport timescale (left panel), the local dynamical timescale (middle), and the gas depletion timescale (right) at different radii from $z \sim 10$ to $z \sim 6$ in the S5-REF simulation. Since there is no well-defined orientation of the gas plane in the simulation, we use the magnitude ratio of vectors $|L|/|\tau|$ as estimates of the timescale for angular momentum change.

is proportional to the local dynamical timescale. Recently, [van de Voort et al. \(2015\)](#) reported that the timescale of this settling can be much longer than the local dynamical timescale if a substantial amount of angular momentum is accreted such as that in mergers, and the gas depletion timescale from observations ranges from 2 Gyr in local spiral galaxies ([Leroy et al. 2008](#)) to 10–100 Myr in starburst galaxies at low- and high- z ([Genzel et al. 2010](#)).

A comparison of the three timescales at different locations and redshifts from the simulation is shown in Figure 4. It is clear that all three timescales show a strong dependence on the distance from the galactic center. While both dynamical and depletion timescales generally show rapid increase with radius, the angular momentum transport timescale increases gradually with radius, reaching a plateau to several Myr at ~ 3 kpc where $t_{\text{dyn}} > 10$ Myr and $t_{\text{dep}} > 100$ Myr, while in the central sub-kpc region it is typically less than 1 Myr, shorter than both dynamical and depletion timescales. The gas depletion timescale quickly increases from ~ 10 Myr at 1 kpc to $\sim 10^3$ Myr at 10 kpc, in good agreement with observations of starburst galaxies ([Genzel et al. 2010](#)), suggesting that star formation in the circumnuclear region is the most efficient.

Figure 4 also shows that all three timescales change with redshift and they become shorter as the galaxy evolves. In particular, the angular momentum timescale decreases across all radii from $z = 10$ and $z = 6$, due to the galaxy interaction and merger during this period as shown in Figure [reffig:gas-star](#). This trend suggests that galaxy interactions can boost efficient angular momentum removal from gas. [Dubois et al. \(2012\)](#) have argued that the low angular momentum gas can be accreted through almost radial cold inflow for high- z galaxies. In our simulation, angular momentum is quickly transported outwards as characterized with the short timescale of several Myrs from the cosmic web to feed the central galaxy. Moreover, the angular momentum transport happens before the net cancellation of angular momentum due to multiple streams as outlined in [Dubois et al. \(2012\)](#). It is likely that the frictional force between the cold inflow and the hot halo gas plays an important role to remove angular momentum in the cold gas streams. Any residual angular momentum is further transported outwards once the gas settles into a rotationally supported disk in the central several kpc region. Since the gas depletion timescale is larger than the other two timescales, the central gas disk is not immediately consumed by star formation but is able to maintain its rotation instead.

The short timescale of angular momentum change facilitates

strong gas inflow to the center, as can be seen from the gas distribution in Figure 3. Following [Muratov et al. \(2015\)](#), the net gas inflow rate can be computed as:

$$\dot{M}_{\text{inf}} = \sum m \frac{\mathbf{v} \cdot \mathbf{r}}{|\mathbf{r}|} \frac{1}{dL}. \quad (13)$$

We computed the net gas inflow rate at different redshifts for a shell between $0.9r$ and $1.1r$ for $r = 0.5, 2.5$, and 10 kpc, respectively, and show the result in Figure 5, in comparison with the star formation rate at each corresponding redshift. Both the inflow rate and SFR increase rapidly during the merger event starting at $z \sim 9.5$, and the gas inflow precedes the star formation. Large inflow rates ($\sim 10^3 M_{\odot}/\text{yr}$) continue from $r = 10$ kpc all the way down to $r = 0.5$ kpc owing to efficient angular momentum transport. Meanwhile, the large inflow of cold gas leads to strong star formation with rates $> 10^3 M_{\odot}/\text{yr}$, in particular within the central 2.5 kpc region. The quasar host in the simulation grows rapidly through intense star formation, and it assembles a stellar population of $\sim 5 \times 10^{11} M_{\odot}$ by $z \sim 6$ as shown in Section 3.3.

The vigorous circumnuclear starbursts in the simulation agree well with the observations of $z \sim 6-7$ quasar hosts, and the extremely high SFRs fall within the measurement range of [Calura et al. \(2014\)](#). This suggests that the extreme starbursts observed in the quasar host galaxies may be triggered by violent galaxy interactions and mergers.

3.2 Growth of the Supermassive Black Holes

Similar to the strong star formation in the host galaxy, the seed BHs grow quickly owing to the abundant gas supply from the filaments in the highly biased region and the frequent interaction and mergers with other protogalaxies, which brings in large gas inflows to the galactic center through efficient angular momentum transport.

Figure 6 shows the growth history of the most massive BH from the simulation. It grows rapidly from $z \sim 13$ to $z \sim 6$ through near-Eddington accretion, boosted by multiple gas-rich mergers during this period. The SMBH assembled a mass of $\sim 6.9 \times 10^8 M_{\odot}$ at $z \sim 7.5$, and $3.9 \times 10^9 M_{\odot}$ at $z = 6.1$, matching the SMBH of the most distant quasar ULAS J1342+0928 at $z = 7.54$, and many bright $z \sim 6$ quasars.

The fact that our simulation produced a SMBH at $z \sim 6$ similar to that [Li et al. \(2007\)](#), who only followed six major mergers from $z = 14.4$ to $z = 6$, highlights the significant role of galaxy interaction

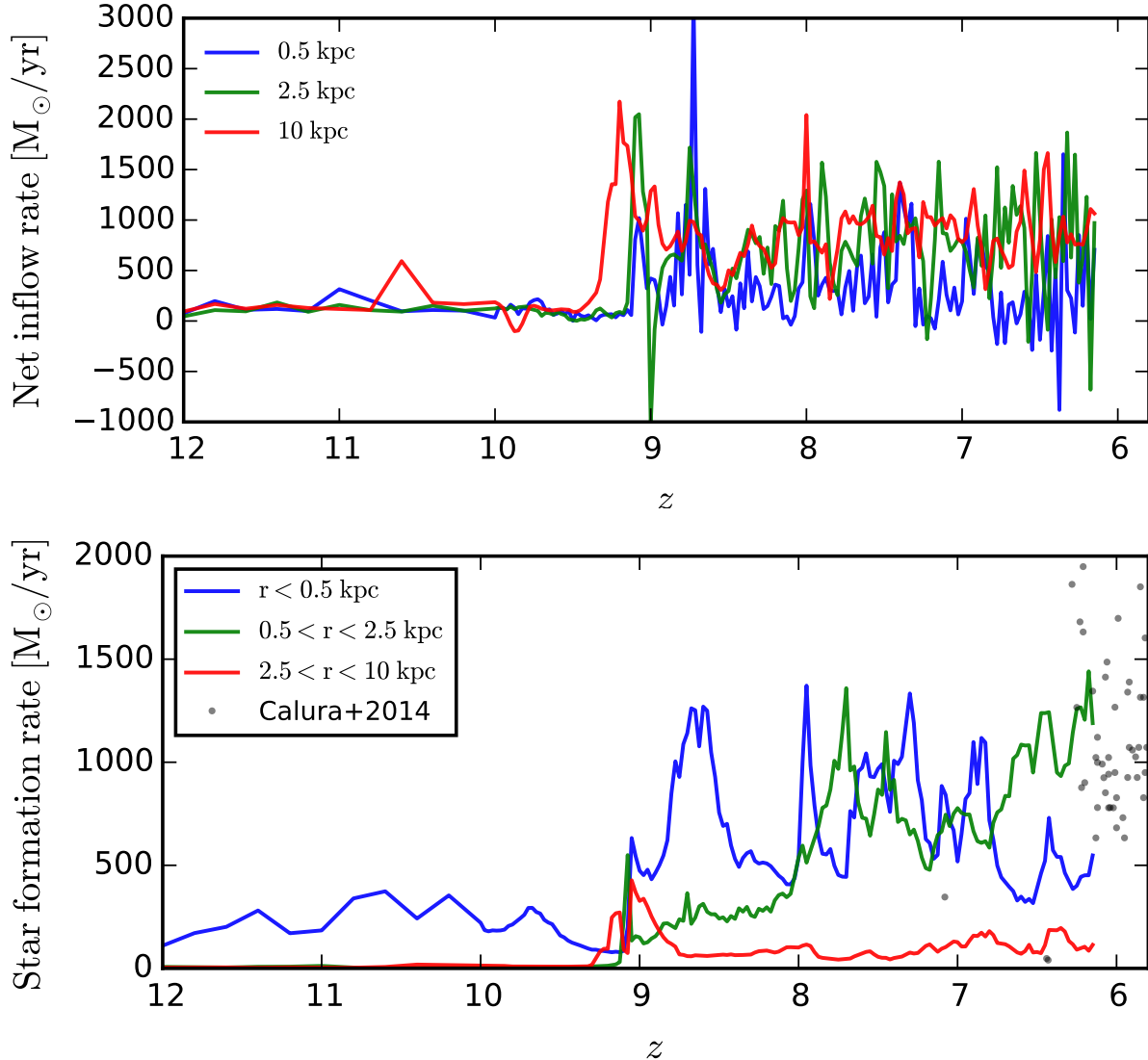


Figure 5. A comparison of the net gas inflow rate (top panel) with the star formation rate (bottom) at different redshifts within three regions at 0.5, 2.5 and 10 kpc from the galaxy center, respectively, from the S5-REF simulation. The grey circles represent observed SFRs of quasar host galaxies at $z \sim 6 - 7$ by Calura et al. (2014).

in BH growth by providing large gas inflow to feed the BHs. We note that although this SMBH underwent multiple mergers, the mass assembled from merged BHs is insignificant compared to its total mass at $z \sim 6$. The most massive BH merger occurred at $z \sim 8.7$ and it acquired a BH of only $1.3 \times 10^6 M_\odot$, about $\sim 1\%$ of its total mass at that time, while most of the BH mergers had large mass ratios > 100 . Our main target is the most massive BH, but the minor mergers may result in the much smaller BHs being kicked out due to large gravitational recoil (Tanaka & Haiman 2009). In total, for this SMBH from the simulation, only $\sim 4 \times 10^6 M_\odot$ came from mergers of BHs, which is $\sim 0.1\%$ of the total BH mass at $z = 6.1$. Therefore, the most important channel for the BH growth in this simulation is gas accretion rather than BH mergers, supporting the previous claim by Li et al. (2007).

The efficient gas accretion by the most massive BH is fueled by dense gas surrounding the BH. As shown in the bottom panel of Figure 6, the gas density around the first progenitor increased rapidly by 4 orders of magnitude from $n_H = 10^1 \text{ cm}^{-3}$ at $z \sim 18$ to

$n_H = 10^5 \text{ cm}^{-3}$ at $z = 12$. Once the gas density rises above $n_H = 10^4 \text{ cm}^{-3}$, the density threshold above which the effective sound speed drops, the Bondi accretion rate would increase (Hopkins & Quataert 2010). Therefore, as demonstrated in the bottom panel of Fig. 6, a combination of a high gas density and low sound speed significantly enhanced efficient gas accretion.

3.3 Host Galaxy of the First Quasar

Along with the intense star formation and BH growth, the host galaxy assembled its mass rapidly through accretion from the dense filaments and a series of mergers with other halos. Figure 7 shows the mass growth history of the main components of the galaxy, including the dark matter, gas, stars and the most massive BH. All the components appear to grow coevally as the host galaxy experiences a series of collisions and mergers with others in the highly overdense environment. These interactions lead to dramatic mass losses and gains, in particular when the galaxy was small at

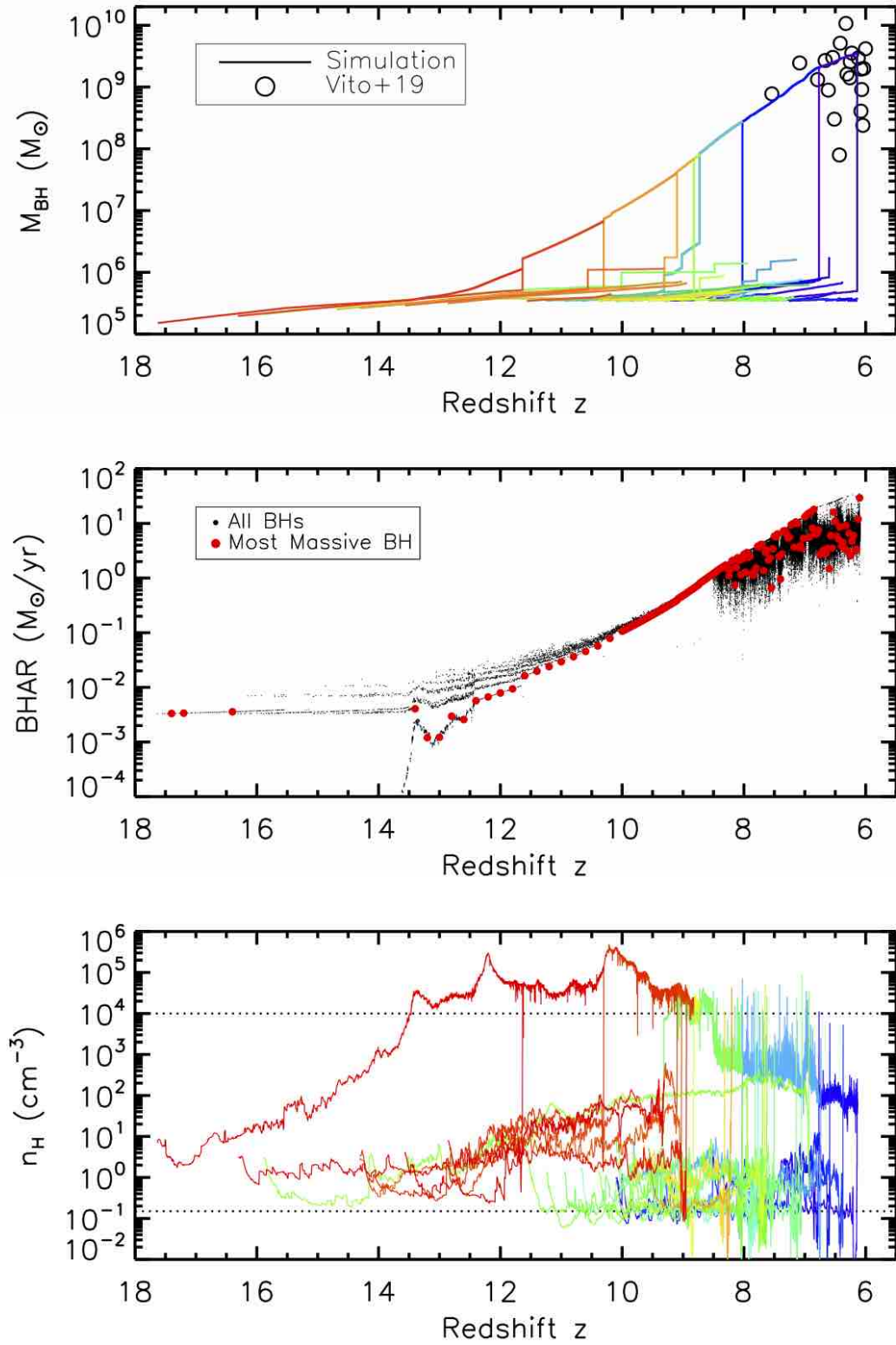


Figure 6. The growth history of the most massive BH from the S5-REF simulation through gas accretion and a series of mergers, in comparison with observations of $z \sim 6$ quasars by Vito et al. (2019) (top panel), the accretion rates of all BHs and the most massive one at different redshifts (middle), and the gas density around each BH before it merged (bottom). The colored lines represent individual BHs merged into the most massive one. In the bottom panel, the upper dashed line indicates the density threshold above which the effective sound speed drops, while the lower one indicates the critical density for star formation. This SMBH assembled a mass of $6.9 \times 10^8 M_{\odot}$ at $z \sim 7.5$, similar to the most distant quasar ULAS J1342+0928 at $z = 7.54$, and $3.9 \times 10^9 M_{\odot}$ at $z \sim 6.1$, matching a number of luminous $z > 6$ quasars such as SDSS J1148+5251 and SDSS J2310+1855 (Vito et al. 2019).

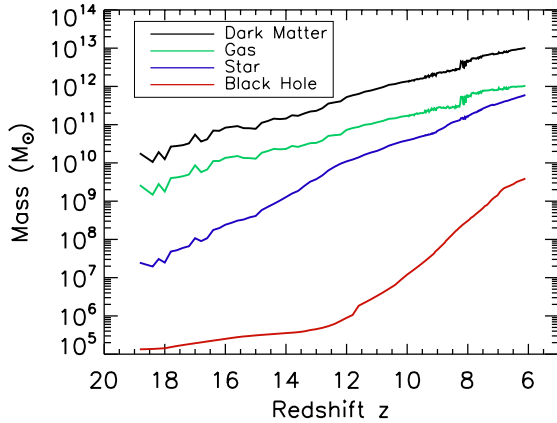


Figure 7. The assembly history of the most massive galaxy in the S5-REF simulation, which hosts the most massive BH at $z \sim 6$. The wiggles show the mass changes during galaxy interactions.

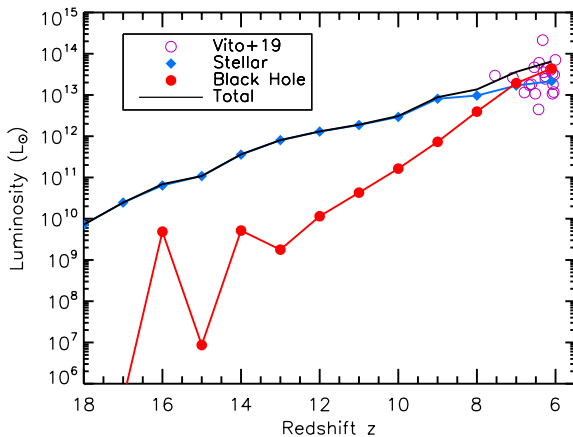


Figure 8. The evolution of luminosities from the stars and the most massive BH, as well as the total of both, for the quasar host galaxy in the S5-REF simulation. The luminosity from stars is calculated using Starburst99 (Leitherer et al. 1999, 2011), while that from the accreting BH is the bolometric luminosity $L_{\text{bol}} = \epsilon_r \dot{M}_{\text{BH}} c^2$. The open circles are bolometric luminosities of $z > 6$ quasars from Vito et al. (2019).

$z > 15$, as evidenced in the wiggles of the mass curves of the gas and stars. After that, the galaxy became more massive and was able to maintain steady growth. The most massive BH grew slowly in the beginning, but starting at $z \sim 13$, its mass growth was accelerated exponentially by rapid accretion fueled by gas-rich mergers. By $z = 6.1$, the galaxy has accumulated $M_{\text{DM}} = 1 \times 10^{13} M_{\odot}$ for dark matter, $M_{\text{gas}} = 9.7 \times 10^{11} M_{\odot}$ for gas, $M_{\star} = 5.9 \times 10^{11} M_{\odot}$ for stars, and $M_{\text{BH}} = 3.9 \times 10^9 M_{\odot}$ for the most massive BH, with a total mass of $M_{\text{tot}} = 1.16 \times 10^{13} M_{\odot}$.

The stellar population grew much faster than the BHs because the star formation rate was much higher than the BH accretion rate during the period $z = 20 - 6$, as shown in Figure 5 and Figure 6. At $z = 6.1$, the SMBH and the host galaxy fall on the local $M_{\text{BH}} - M_{\star}$ correlation suggested by Kormendy & Ho (2013), as shown in Section 4.5.

Figure 8 shows the evolution of the luminosity of the quasar host galaxy, with contributions from both the stars and the most

massive BH. From early on, the luminosity of the host is dominated by stellar radiation until $z \sim 7$, when the BH catches up and outshines the stars. At $z = 6.1$, the SMBH accretes at a rate of $\dot{M}_{\text{BH}} = 29 M_{\odot}/\text{yr}$ and produces a luminosity of $L_{\text{AGN}} = 4.3 \times 10^{13} L_{\odot}$ assuming a radiative efficiency $\epsilon_r = 0.1$. By taking into account the emission of $L_{\star} = 2.2 \times 10^{13} L_{\odot}$ from young stars calculated using Starburst99 (Leitherer et al. 1999, 2011), this galaxy would shine brightly with a total luminosity of $L_{\text{tot}} = 6.5 \times 10^{13} L_{\odot}$ at $z \sim 6$, making it a highly luminous quasar like SDSS J1148+5251 and SDSS J2310+1855 (Vito et al. 2019). Moreover, this galaxy reaches $L_{\text{tot}} \sim 10^{12} L_{\odot}$ by $z \sim 12$, which would represent a starbursting galaxy with a buried AGN in the early stage of the cosmic reionization. Therefore, this simulation offers valuable insights into the formation and evolution of the first galaxies and quasars. In a companion study (Li et al. in prep), we perform multi-wavelength radiative transfer post-processing on the S5-REF and other simulations to derive the panchromatic properties of $z > 6$ quasar hosts for direct comparison with multi-band surveys.

After the completion of the last major merger at $z \sim 7$, the host galaxy remains isolated for a period of time. A disk of rotating gas formed within the center of the galaxy potential. Newly born stars trace closely the prominent spiral arms within the gas disk. At $z = 6.1$, the host galaxy exhibits a bright concentrated bulge with old stars and a more extended (5 kpc in size) young stellar population.

To study the structural properties of the host galaxy, we compute the circular velocity, $v_c = (GM(<r)/r)^{1/2}$, of the galaxy and the contribution from each component, as shown in Figure 9. We also include the circular velocity curves of the same halo from a dark matter - only (DMO) simulation for comparison. There is already a noticeable difference in v_c at redshifts as early as $z = 14$ where the maximum circular velocity v_{max} in the hydrodynamic simulation is larger than that in the DMO run, the distribution of dark matter in the hydrodynamic simulation shows clear enhancement in the central region, and the gap of v_c in the central region between the two simulations continues to increase with time.

Starting from $z = 12$, the mass distribution in the central regions is dominated by baryons (stars and gas) rather than dark matter. The size of the baryon-dominated region increases from 1 kpc at $z = 12$ to 6 kpc at $z = 6.5$. Instead of a flat rotation curve as in the DMO simulation, the galaxy in the S5-REF simulation shows a strong Keplerian falloff from the central kpc to the outer radius. The rotational curves at $z = 6.5$ suggest that the galaxy is compact, with a stellar mass of $\sim 4 \times 10^{11} M_{\odot}$ within the central 2.5 kpc.

The stellar mass of the galaxy at $z = 6.1$ in the S5-REF simulation is similar to that of previous hydrodynamic simulations (Li et al. 2007; Khandai et al. 2012; Feng et al. 2014; Lupi et al. 2019) and to semi-analytical modeling Valiante et al. (2014, 2016); Pezzulli et al. (2016). However, the compact size of the galaxy only signifies a mass discrepancy discussed in Valiante et al. (2014). Recent measurements of gas kinematics of quasar hosts suggest that the inferred dynamical mass is $\sim 10^{10} - 10^{11} M_{\odot}$ (Wang et al. 2010, 2013). Besides the effects of inclination of a $\sin^2(i)$ factor or the ‘‘Lauer bias’’ (Lauer et al. 2007), another way to reduce this tension is to postulate that the stellar distribution is extended into tens of kpc as seen in Khandai et al. (2012). However, an extended stellar distribution contradicts with the concentrated distribution in our simulation. It is thus crucial to determine whether the majority of high- z quasar hosts are viewed face-on (Ho 2007). Moreover, recent simulations by Lupi et al. (2019) suggest that the galaxy mass in high- z quasars observations is based on gas tracers that underestimate the true mass, which may explain the tension between models

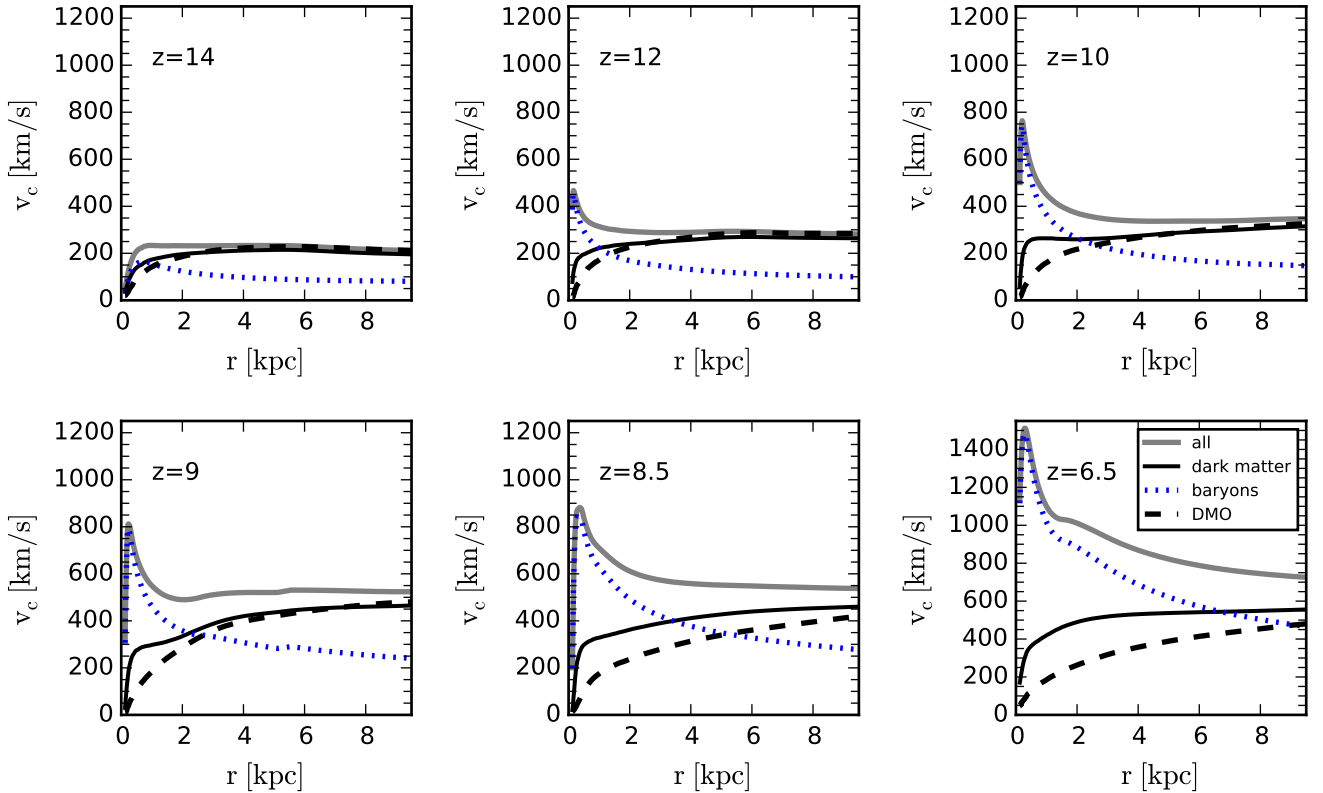


Figure 9. The circular velocity curves of the quasar host galaxy from $z = 14$ to $z = 6.5$ in the S5-REF simulation. For comparison, contributions from dark matter (black line) and baryons (blue dotted line) are shown, as well as the circular velocity curves of the same halo from a dark matter - only (DMO) simulation (black dashed line). $v_c(r)$ from $z = 14$ to $z = 6.5$.

and observations. We will investigate this issue in a companion paper using the emission lines from radiative transfer calculations (Li et al. in prep).

The presence of massive galaxies at high- z has already been reported in the literature (e.g. Mobasher et al. 2005; Wiklind et al. 2008; Marchesini et al. 2010; Stefanon et al. 2015). It was argued that the majority of the stellar mass should be formed very rapidly in a manner similar to the monolithic collapse model (Eggen et al. 1962), and that the rapid assembly of large stellar masses poses considerable challenges to the hierarchical structure formation model (Steinhardt et al. 2016; Glazebrook et al. 2017). However, our results show that massive galaxies and hosts of luminous quasars can grow rapidly through accretion from filaments in a highly biased region and frequent mergers in a standard cosmological model of hierarchical structure formation. We will study the host galaxies of $z > 6$ quasars with a sample of 30 cosmological zoom-in simulations of different halos (Zhu et al. in prep).

4 TEST OF MODELS AND PARAMETERS

In this Section, we present results of the 15 simulations listed in Table 1 to test a number of models and parameters, including BH seeds with $M_{\text{seed}} = 10^1 - 10^6 M_\odot$, Eddington limits with $\max(\lambda_{\text{Edd}}) = 1 - 10^4$, feedback from both constant- ϵ_r , radiative-efficient accretion and varying- ϵ_r from super-critical accretion models, as well as Bondi accretion variations, and cosmological parameters. We will identify the viable models for $z \sim 6$ quasars with

$10^9 M_\odot$ SMBHs. All these simulations use the same galaxy halo as S5-REF, as described in the previous Section 3.

4.1 The BH Seed Models

We test all three seed scenarios described in Section 2.3: light seeds with $M_{\text{seed}} = 10$ and $10^2 M_\odot/h$, respectively; intermediate seeds of 10^3 and $10^4 M_\odot/h$, respectively; and heavy seeds of 10^5 and $10^6 M_\odot/h$, respectively. The light seeds are assumed to be remnants of Pop III stars formed from metal poor gas of $Z < 10^{-4} Z_\odot$, so in the simulations they were created 2 Myrs after the Pop III stars formed. For the intermediate and heavy seeds, since the initial conditions of their formation are not well constrained, we adopt the same scheme to plant the seed in $10^{10} M_\odot/h$ halos so we can compare the results directly. In the simulation, the first Pop III star formed at redshift $z \sim 26$, and the first halo reached $10^{10} M_\odot/h$ at $z \sim 19$. For the simulations in this test, the light seeds were modeled with super-critical accretion with spin $a = 0$, while the heavy seeds used the conventional Eddington-limited, thin-disk model with radiative efficiency $\epsilon_r = 0.1$ (a comparison between thin-disk and super-critical accretion for the heavy seeds is presented in Section 4.3).

A comparison of the seed models is shown in Figure 10 with the six simulations S1, S2, S3, S4, S5-REF and S6, which correspond to the BH seed mass of 10, 10^2 , 10^3 , 10^4 , 10^5 , $10^6 M_\odot/h$, respectively. The left panel shows the BH mass growth history of each seed model in comparison with BH masses of $z > 6$ quasars measured by Vito et al. (2019), as well as those converted from UV luminosity M_{1450} by Inayoshi et al. (2020) for the complete sample of 203 $z \gtrsim 6$ quasars. As the curves demonstrate, small seeds S1, S2 and S3

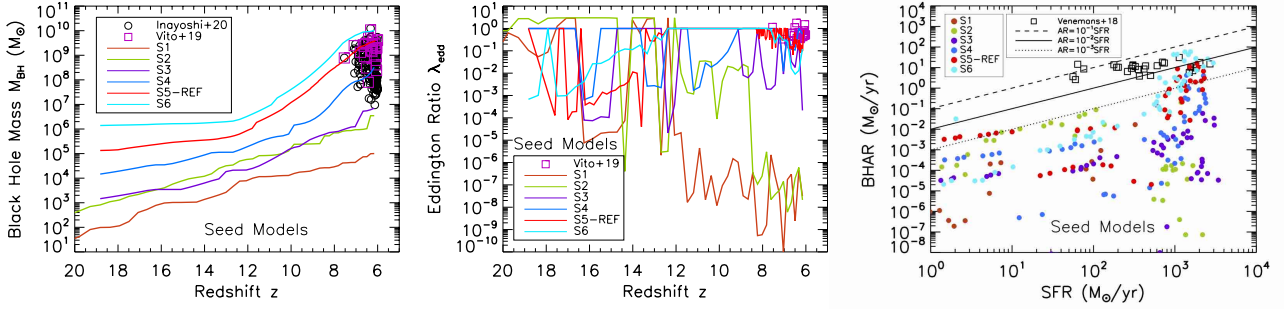


Figure 10. A comparison of the Seed Model simulations with BH seed masses of $10, 10^2, 10^3, 10^4, 10^5$ and $10^6 M_{\odot}/h$, corresponding to S1, S2, S3, S4, S5-REF and S6, respectively, as listed in Table 1. Note the BH properties in the plots refer to the most massive BH in each simulation, and each colored line or circle represents a specific simulation as indicated in the legend. *Left panel:* The BH mass growth history from each simulation in comparison with measurements of 25 $z > 6$ quasars from Vito et al. (2019), and those converted from UV luminosity M_{1450} of the complete sample of 203 $z \geq 6$ quasars from Inayoshi et al. (2020). *Middle panel:* Evolution of Eddington ratio of the BH accretion from each simulation in comparison with observations from Vito et al. (2019). *Right panel:* Relation between the BH accretion rate and the star formation rate of the host galaxy from each simulation, in comparison with observations from Venemans et al. (2018), and scaling relations of $\text{AR} = 10^{-1}, 10^{-2}, 10^{-3} \text{SFR}$, as represented by the black dashed, solid and dotted lines, respectively.

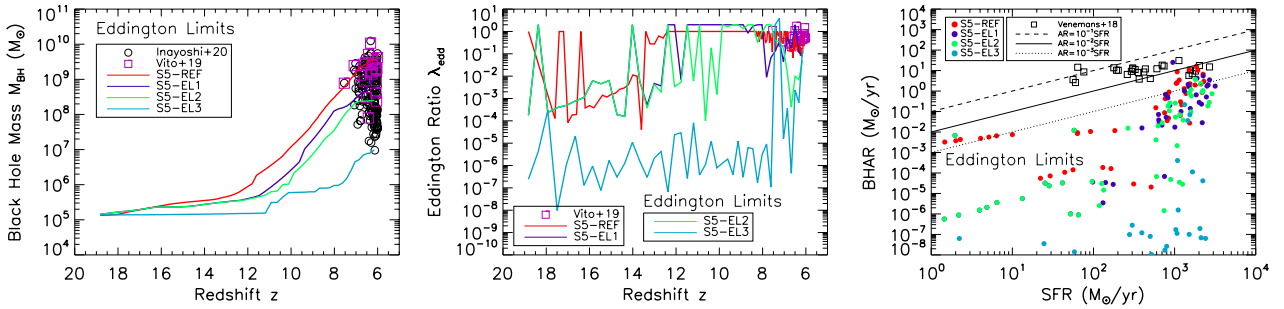


Figure 11. Same as Figure 10, but for simulations with different maximum Eddington limits: $\max(\lambda_{\text{Edd}})=1$ (Eddington limited, S5-REF), 2 (super-Eddington, S5-EL1), 5 (super-Eddington, S5-EL2), and 10^4 (hyper-Eddington, S5-EL3), respectively.

grow slowly with a shallow slope, while big seeds S4, S5-REF and S6 grow exponentially from $z \sim 12$ on after an initial slow phase. At $z = 6.1$, the most massive BH of the S1 - S6 simulation grows to $\sim 10^5, 3.6 \times 10^6, 7 \times 10^6, 3.3 \times 10^8, 5.3 \times 10^9, 1 \times 10^{10} M_{\odot}$, respectively. The small seeds S1 - S3 fail to reach the BH mass threshold of $10^7 M_{\odot}$ of the quasars detected at $z > 6$, while the bigger seeds S4 - S6 produce SMBHs in the mass range of the observed $z > 6$ quasars, with S4 at the lower end and S6 on the high end above all but one, nearly matching the SMBH of SDSS J0100+2802 at $z = 6.31$, the most massive SMBH in the early Universe (Wu et al. 2015). The S5-REF appears to be the most successful model of the six in the test, producing a SMBH close to that of the most distant quasar ULAS J1342+0928 at $z = 7.54$ (Bañados et al. 2018), and numerous luminous quasars at $z \sim 6$ (Vito et al. 2019).

The middle panel of Figure 10 shows the Eddington ratio of each model as a function of time. All models have highly fluctuating accretion rates, although bigger seeds are able to maintain higher rates than the smaller ones. Even though S1 and S2 were run with the super-critical accretion model, both had only brief periods of super-Eddington accretion in the beginning, then dropped to sub-Eddington after $z \sim 12$ when multiple galaxy mergers took place; especially S1 dropped by nearly 9 orders of magnitude. The big seeds typically had $\lambda_{\text{Edd}} \gtrsim 10^{-3}$, in particular S5-REF and S6 had

near-Eddington accretion for a significant fraction of the time, and the Eddington ratios are in good agreement within the range of $\lambda_{\text{Edd}} \sim 0.1 - 2$ of quasars at $z \sim 6 - 7.5$ (Vito et al. 2019).

The right panel of Figure 10 shows the relation between the accretion rate of the most massive BH and the SFR of the host galaxy from simulations S1 - S6, in comparison with measurements of $z \geq 6$ quasars from Venemans et al. (2018) in which the SFR was derived from the far-infrared luminosity while the BH accretion rate was estimated from the bolometric luminosity assuming $\epsilon_{\text{r}} = 0.1$ (Decarli et al. 2018). The hosts of the observed $z \geq 6$ quasars are strong starbursts with $\text{SFR} \sim 50 - 3000 M_{\odot}/\text{yr}$, and the BH accretion rates (BHARs) reach $\sim 5 - 40 M_{\odot}/\text{yr}$. These observed quasars fall in the range of $10^{-3} \text{SFR} \lesssim \text{BHAR} \lesssim 10^{-1} \text{SFR}$. In our modeling, the host halo is the same for all the simulations, and it is a strong starbursting galaxy as shown in Section 3 with $\text{SFR} \sim 300 - 1400 M_{\odot}/\text{yr}$ at $z \sim 6 - 7$, agreeing with observed $z \geq 6$ quasar hosts. The BH accretion, however, differs significantly from model to model. S1 - S3 models have low BH accretion rates $< 10^{-2} M_{\odot}/\text{yr}$ most of the time, while S4 - S6 have higher rates than the lighter seeds, in particular during $z \sim 6 - 7$, S5-REF and S6 have rates $\sim 1 - 30 M_{\odot}/\text{yr}$, and they fall in the range of $10^{-3} \text{SFR} \lesssim \text{BHAR} \lesssim 10^{-1} \text{SFR}$ like the observed $z \geq 6$ quasars.

We note that the Simba simulation (Davé et al. 2019) produced the same linear $\text{BHAR} - \text{SFR}$ correlation from $z \sim 5$ to $z \sim 0$

(Thomas et al. 2019). This is because in their model, the BHAR estimator scales linearly with the gravitational torque-limited gas inflow rate, with which the SFR also scales linearly. In our simulations, as we show in Figure 5, the SFR follows closely with the gas inflow rate, however, as shown in Figure 10, the BHAR does not scale linearly with SFR, and the $z \sim 6$ quasar observations by Venemans et al. (2018) do not show a linear $BHAR-SFR$ correlation. Furthermore, analysis by Pensabene et al. (2020) suggest that $z \sim 6$ quasars do not follow the same $M_{BH}-M_{\star}$ correlation as local galaxies.

The two light seed simulations ($M_{seed}=10, 100 M_{\odot}$) were indeed run with the super-critical slim-disk model, and they did have super-Eddington accretion, although for some short periods only, as shown in the middle panel of Fig 10. The accretion history is rather chaotic, and the radiative efficiency fluctuates quite widely with the BH mass and accretion rate, so the growth is not steady as the semi-analytical calculations even with the super-critical mode. Resolution is certainly a big concern here as we cannot resolve these light seeds and the gas density around them, so it is possible that the accretion rate is underestimated.

Overall, it is clear from Figure 10 that the BH growth path and final mass depend strongly on the seed BH mass. In contrast to previous studies (e.g., Madau et al. 2014; Volonteri et al. 2015), our simulations show that light seeds of $10, 10^2 M_{\odot}$ from Pop III remnants fail to grow to $10^7 M_{\odot}$ even with the super-critical accretion model due to strong feedback. Both models reach super-Eddington accretion, but for some short periods and with large fluctuations. The chaotic growth is not steady as is typically assumed in the semi-analytical calculations. The accretion rates may be underestimated due to our limited resolution as we cannot resolve the gas density around the BHs, but similar results were also reported by other studies with different resolutions (e.g., Lupi et al. 2016; Smith et al. 2018). In particular, Smith et al. (2018) followed the growth of over 15000 BHs from Pop III stars in the Renaissance simulations with ultra-high resolutions down to $m_{DM} = 1.27 M_{\odot}/h$, and they found inefficient growth for most of the BHs, with an average mass increase less than 10%. On the other hand, the bigger seeds of $10^4 - 10^6 M_{\odot}$ were able to achieve higher rates than the smaller ones and maintain near-Eddington accretion for a substantial period of time, enabling them to grow to $10^8 - 10^9 M_{\odot}$ by $z \sim 6$, in agreement with other simulations (e.g., Sijacki et al. 2009; Dubois et al. 2013; Costa et al. 2014; Feng et al. 2014; Curtis & Sijacki 2016a; Smidt et al. 2018; Huang et al. 2020). The $10^3 M_{\odot}$ seed was planted using the same scheme as the heavy ones in our simulations for a head-to-head comparison, and it grew to $\sim 10^7 M_{\odot}$ at $z \sim 6$, bridging the gap between the Pop III and direct collapse BHs, although Huang et al. (2020) suggested that they could grow to $10^8 - 10^9 M_{\odot}$ if they were seeded in smaller halos formed at earlier times.

The finding of the BH seed tests highlights the need of heavy seeds for the formation of the luminous quasars observed at $z \sim 6$ in the standard structure formation model, motivating more theoretical and observational investigations on the formation of heavy BH seeds in the early Universe.

4.2 The Eddington Limit

In order to explain the rapid formation of $\sim 10^9 M_{\odot}$ SMBHs within the first billion years, super- or hyper-Eddington accretion has been proposed (e.g., Pacucci et al. 2015; Inayoshi & Haiman 2016; Lupi et al. 2016; Ryu et al. 2016; Pezzulli et al. 2016; Sugimura et al. 2017; Becerra et al. 2018; Takeo et al. 2019). However, some recent simulations suggested that feedback from super-Eddington accre-

tion would suppress BH growth (e.g., Smith et al. 2018; Regan et al. 2019). Here we test the effects of the Eddington limit on the growth of BHs by varying the free parameter $\max(\lambda_{edd})$.

Figure 11 shows a comparison of the four simulations S5-REF, S5-EL1, S5-EL2, and S5-EL3, which correspond to $\max(\lambda_{edd})=1, 2, 5$, and 10^4 , respectively. Similar to Figure 10, the left panel shows the BH mass growth history of each simulation in comparison with BH masses of $z > 6$ quasars from Vito et al. (2019) and Inayoshi et al. (2020).

Counter-intuitively, Figure 11 shows that a higher maximum Eddington rate leads to a lower BH mass growth; while the fiducial model with $\max(\lambda_{edd})=1$, S5-REF produced a SMBH of $5.3 \times 10^9 M_{\odot}$ at $z = 6.1$, the Hyper-Eddington model with $\max(\lambda_{edd}) = 10^4$ produced the least massive BH of $\sim 10^7 M_{\odot}$, more than two orders of magnitude lower than that of S5-REF $\max(\lambda_{edd}) = 1$, due to strong feedback. This test of Eddington limits demonstrates the self-regulating of the growth rate of BHs by radiation feedback.

4.3 The Radiative Feedback Models

To study the impact of feedback from an accreting BH on its own growth, we test two widely considered feedback mechanisms: the radiative-efficient thin-disk model with constant ϵ_r , and a super-critical slim-disk model with varying ϵ_r depending on the BH mass, accretion and spin, as described in Section 2.5.

Figure 12 shows a comparison of the four simulations S5-REF, S5-FB1, S5-FB2, and S5-FB3, which correspond to simulations run with thin disk accretion with $\epsilon_r = 0.1$, super-critical accretion with varying ϵ_r for spin $a = 0$, $a = 0.99$, and thin disk $\epsilon_r = 0.2$, respectively. Similar to Figure 10, the left panel shows the BH mass growth history of each simulation in comparison with BH masses of $z > 6$ quasars from Vito et al. (2019) and Inayoshi et al. (2020).

Clearly, the radiative efficiency ϵ_r has a significant impact on the BH growth. For the thin-disk model, the final mass of S5-FB3 with $\epsilon_r = 0.2$ is only $\sim 3.9 \times 10^7 M_{\odot}$, which is lower than that of the fiducial model S5-REF with $\epsilon_r = 0.1$ by nearly two orders of magnitude. For the slim-disk model, S5-FB1 ($a = 0$) reaches $\sim 8.3 \times 10^9 M_{\odot}$, which is more than one order of magnitude larger than the $\sim 5.7 \times 10^8 M_{\odot}$ of S5-FB ($a = 0.99$), as the latter has higher radiative efficiency due to higher spin. Owing to low radiative efficiency ($\epsilon_r < 0.01$), the BH in S5-FB1 grows rapidly with super-critical accretion with an Eddington ratio $\max(\lambda_{edd}) = 2.6$, as shown in the middle panel of Figure 12. During the super-Eddington accretion phase around $z \sim 7 - 10$, the most massive BH in S5-FB1 reaches extremely high accretion rates $BHAR \sim 10^4 M_{\odot}/yr$, which is significantly larger than those of $z \sim 6 - 7$ quasars estimated by Venemans et al. (2018), as shown in the right panel of Figure 12. As a result of super-Eddington accretion with low radiative efficiency, S5-FB1 produces the most massive BH among all the S5 simulations with the same BH seed, with $M_{BH} = 8.3 \times 10^9 M_{\odot}$.

4.4 Bondi Accretion Variations

To compare the different Bondi accretion models employed in various cosmological simulations, Figure 13 shows the results from simulations using three models: our chaotic cold accretion model as in the fiducial run (S5-REF), the conventional model of Di Matteo et al. (2005) with constant $\alpha = 100$ (S5-BA1), and the model of Booth & Schaye (2009) with a power-law α (S5-BA2). The overall growth of BH mass in these three models is in good agreement with

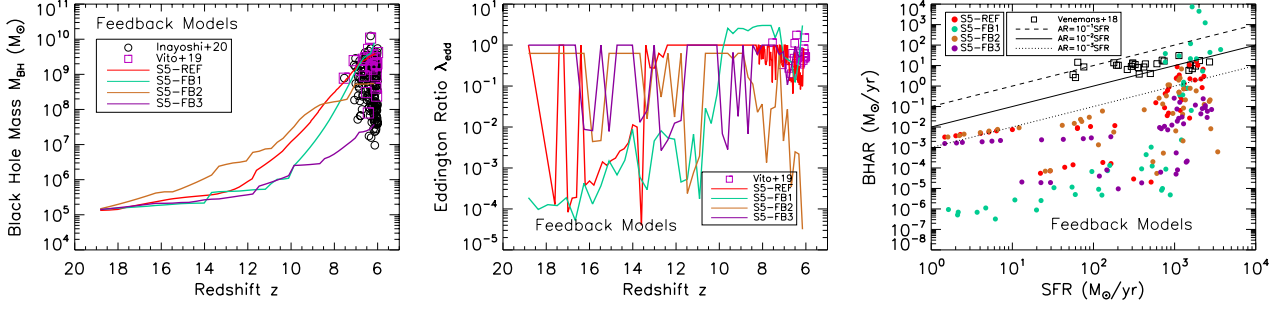


Figure 12. Same as Figure 10, but for simulations with different accretion and feedback models: thin disk accretion with $\epsilon_r = 0.1$ (S5-REF), super-critical accretion with varying ϵ_r for spin $a = 0$ (S5-FB1), $a = 0.99$ (S5-FB2), and thin disk $\epsilon_r = 0.2$ (S5-FB3), respectively.

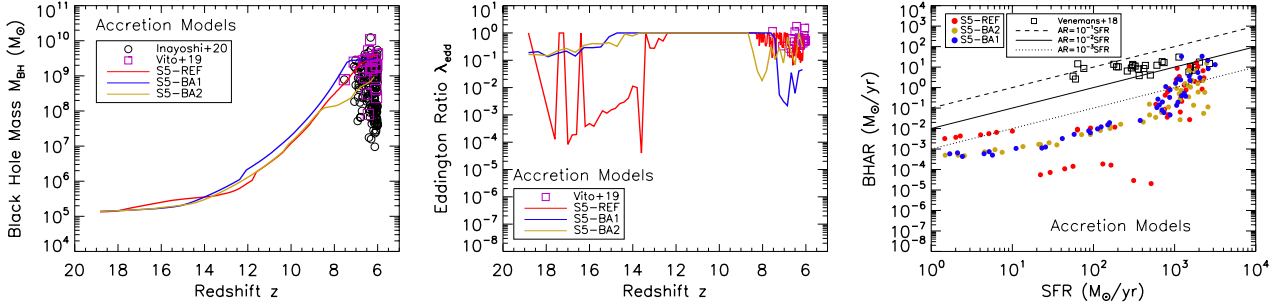


Figure 13. Same as Figure 10, but for simulations with different parameters for the Bondi accretion: chaotic cold accretion (S5-REF), and conventional Bondi accretion with constant $\alpha = 100$ (S5-BA1), and power-law α (S5-BA2).

each other. As shown in the left panel of Figure 13, the S5-REF produces the most massive BH of the three, with $M_{\text{BH}} \sim 3.9 \times 10^9 M_\odot$, while that of S5-BA1 is slightly smaller with $M_{\text{BH}} \sim 3 \times 10^9 M_\odot$, followed by S5-BA2 with $M_{\text{BH}} \approx 10^9 M_\odot$. The detailed accretion of the BHs differs, however, as shown in the middle panel of Figure 13, where S5-REF shows a more chaotic growth history, in particular in the early phase at $z > 14$, which results in lower accretion rates, as shown in the right panel of Figure 13, but it becomes more stable at later times. All three simulations have a substantial period of near-Eddington accretion, which is critical to produce $\sim 10^9 M_\odot$ SMBHs at $z > 6$.

We have also run the simulation with different cosmological parameters: WMAP 5-year results and Planck 2016 cosmology, respectively, but there is no significant difference in the BH growth histories and other results, as we will show in the next Section.

4.5 Viable Models for the $z \sim 6$ Quasars with $10^9 M_\odot$ SMBHs

To explore the viable paths to produce $\sim 10^9 M_\odot$ SMBHs at $z \gtrsim 6$, we examine the duty cycle of Eddington accretion of the BHs, f_{duty} , as in Equation (1). Figure 14 shows the correlation between the final BH mass from the simulations and the duty cycle f_{duty} , with a fitting function $f_{\text{duty}} = 0.086 \log(M_{\text{BH}}) - 0.31$. This correlation suggests that the BH mass growth scales exponentially with f_{duty} , so the longer a BH stays in the near- or super-Eddington accretion phase, the more rapidly it accumulates its mass. Figure 14 also shows that heavy BH seeds of $\gtrsim 10^5 M_\odot$ can grow to $10^9 M_\odot$ by $z \sim 6$ in both thin- and slim-disk models, provided that the duty cycle of near-Eddington accretion with an Eddington ratio $\lambda_{\text{Edd}} \gtrsim 0.6$ is maintained at $\gtrsim 40\%$.

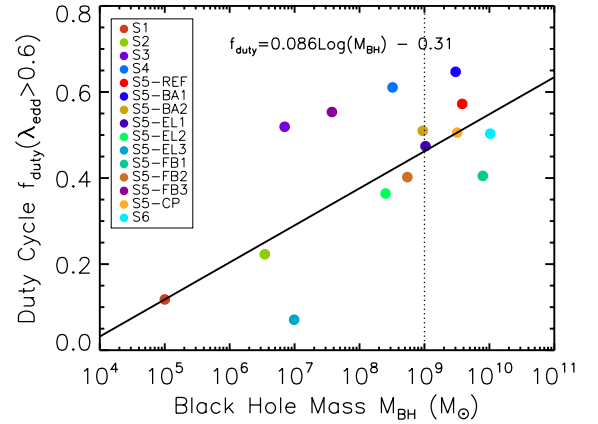


Figure 14. The correlation between the duty cycle of near-Eddington accretion and the final BH mass of all simulations in this study.

Figure 15 shows the correlation between the final BH mass and the stellar mass of the host galaxy, throughout the assembly history until $z = 6.1$ for all simulations in this work. In most cases, BHs start to grow more efficiently when the galaxy stellar mass exceeds $3 \times 10^{10} M_\odot$, corresponding to $z \sim 12$ when the host progenitor experiences major galaxy collisions. Compared to the local observed correlations, $M_{\text{BH}} - M_\star$, of ellipticals (Kormendy & Ho 2013) and AGNs (Reines & Volonteri 2015), the growth curves of these early

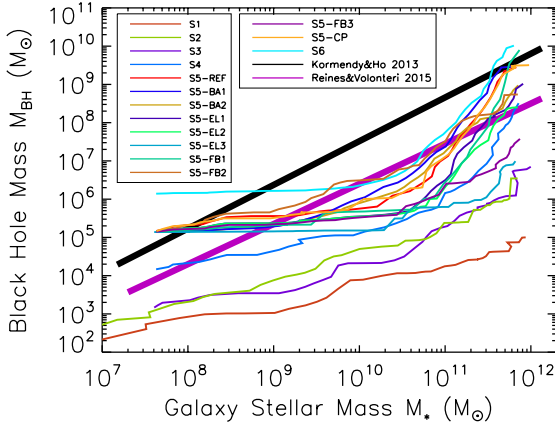


Figure 15. The correlation between BH mass M_{BH} and galaxy stellar mass M_* across the growth history of all simulations in this study, in comparison with observed correlations of local ellipticals by Kormendy & Ho (2013) and local AGNs by Reines & Volonteri (2015).

quasars do not follow the local $M_{\text{BH}} - M_*$ relations, although at $z = 6.1$, several models (S5-REF, S5-BA1, S5-CP, S5-FB1, S6) appear to fall on that of the local ellipticals, while S4, S5-EL1, S5-BA2, S5-EL2, and S5-FB2 fall on that of the local AGNs. This plot demonstrates that even with the same host galaxy, the BH growth history varies significantly with different seeds, therefore they may have different $M_{\text{BH}} - M_*$ relations at different stages of growth.

As demonstrated in Figure 15, the BH masses always catch up with the host galaxy mass, a feature that is not that surprising for our model. Recall that in the previous sections we show that most BH growth occurs between $z \sim 12$ and 7, determined by efficient gas inflow. It is only when the BH is massive enough so that its energetic feedback can effectively halt the gas accretion. By then, much of the gas has fueled intense star formation in the inner 2.5 kpc. Despite the differences in the seed mass or radiative efficiencies, there is no alternative route directly to feed the central BH without making stars along the way.

5 DISCUSSION

While our simulations provide a number of new insights on the formation of the first SMBHs and quasars, there are caveats as in other simulations. In this section we discuss the limitations of our modeling and comparisons with previous studies.

5.1 Limitations of Numerical Methods

We stress that the models of star formation, BH accretion, and feedback from both supernovae and AGNs are all *phenomenological* descriptions, that the sub-grid recipes we employ to follow these processes in cosmological simulations are *simplified* approaches, and that the numerical methods and resolution are *limited* by the computational resources.

It is computationally prohibitive to achieve sufficient numerical resolution to resolve individual stars or small BHs in cosmological simulations on ~ 10 Mpc scales, and so our resolution is far from resolving the BH seeds in the simulations. Smith et al. (2018) compared the growth of BHs from Pop III remnants in the

Renaissance simulations, which have a dark matter mass resolution of $m_{\text{DM}} = 2.9 \times 10^4 M_{\odot}/h$, to that from Pop2Prime simulations (Smith et al. 2015) which have extremely high resolution ($m_{\text{DM}} = 1.27 M_{\odot}/h$), and found that the average accretion rate increased from $\sim 10^{-15} M_{\odot}/\text{yr}$ to $\sim 10^{-13} M_{\odot}/\text{yr}$ when the resolution increased by 4 orders of magnitudes. However, such an extreme regime with extremely low accretion is beyond the scope of our study, because the frequent hierarchical mergers of the halo in our simulations provide abundant gas supply and efficient angular momentum transport to fuel intense starbursts with star formation rates up to $10^3 M_{\odot}/\text{yr}$ and high BH accretion rates of $\sim 10^{-3} - 30 M_{\odot}/\text{yr}$, as shown in Section 3.

As mentioned in Section 2, another significant challenge of this project is the treatment of small BHs of $10 - 100 M_{\odot}$ from Pop III stars in simulations with mass resolution of $\sim 10^5 - 10^6 M_{\odot}$, because the large mass ratio between particles would cause two-body heating and other numerical issues. To alleviate the problem, we adopted a numerical technique to treat the BH as a fraction of the parent Pop III star particle from which the BH formed, such that the BH particle will have the same dynamics as its parent star particle while maintaining its own mass and accretion activity. This technique is similar to that used by Springel & Hernquist (2003) to treat star formation in which a fraction of the gas particle becomes the new star, reducing two-body relaxation as the star particles have comparable mass to other particles, and it enables the small BHs to evolve robustly and with a growth history consistent with other massive BHs, as described in Section 2.3.1.

Recent developments, such as super-Lagrangian refinement (Curtis & Sijacki 2015) will be of great help to resolve the gas angular momentum before it reaches the accretion radius of the BH. In addition, quantities such as BH mass and accretion rate are less likely to be numerically converged than quantities such as the stellar mass (Sijacki et al. 2015). As the BH physics is always carried out on the resolution scale (grid size Δx or smoothing length h), accurate modeling of BH growth in cosmological simulations may remain a significant challenge in the near future (Wurster & Thacker 2013).

5.2 Caveats of Physical Models

As we show in the model comparison section, BH mass is sensitive to model parameters such as the seed mass, seed halo mass, radiative efficiency, and the maximum Eddington ratio. Our model of BH accretion rate is based on the Bondi-Hoyle formula with several different estimates of boost factors, although the differences are found to be small due to the fact that most efficient mass growth period is Eddington-limited. However doing this, we ignore the dependence on gas angular momentum (Curtis & Sijacki 2016b; Negri & Volonteri 2017; Anglés-Alcázar et al. 2017).

Since we focus on the bright quasar phase of the BHs in this study, only quasar mode feedback is included in our simulations. We do not include radio feedback where jets or outflows from BHs at low state inflate giant radio lobes. Radio feedback model (Sijacki et al. 2007; Dubois et al. 2011; Weinberger et al. 2017) is now routinely used in the current simulations (Vogelsberger et al. 2014a; Kaviraj et al. 2017; Pillepich et al. 2018a). We justify our choice of not modeling radio mode because the presence of radio-loud quasars at $z \geq 4$ is generally very rare (Volonteri & Stark 2011; Yi et al. 2014). Using numerical simulations, Sijacki et al. (2015) also found that for the most massive BHs, the mean Eddington ratio consistently drops from $z = 4$ to 0, a signature of cosmic downsizing. Therefore, the radio mode feedback would be insignificant in the early quasars.

In our simulations, BH kick from velocity recoil during BH–

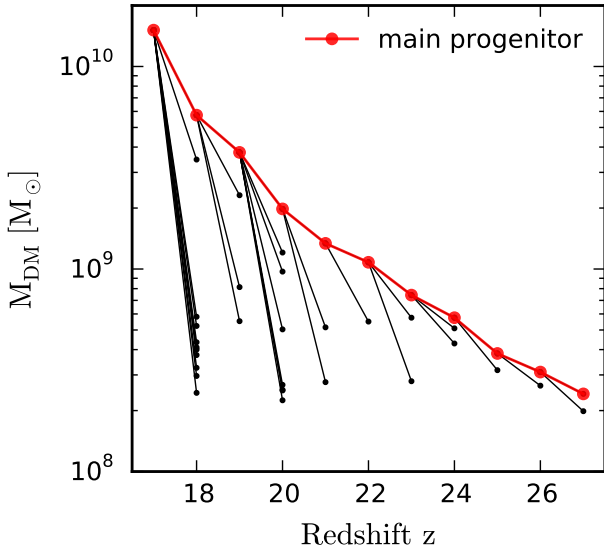


Figure 16. Merger tree of the dark matter halo from redshift $z = 27$ to 17 , when the first BH is seeded at $M_{200} = 10^{10} M_{\odot}/h$. The main progenitor is shown by the solid red symbols while the small symbols indicate the dark matter halos that merged with the main progenitor. There are 30 dark matter halos in total with mass above $10^8 M_{\odot}$ that merged between $z = 27$ and 18 .

BH mergers is not included. The circular velocity curve of the central galaxy has reached $\sim 800 \text{ km s}^{-1}$ already at $z = 10$. In addition, the mass ratios of the BH–BH mergers are generally very low. The impact of any kick from gravitational recoil would be minimal. Furthermore, the strong gas drag force due to the presence of the gas disk also damps any kick substantially, so BH kick would not affect the growth of the most massive BHs we present here.

It is useful to examine how well the BH seed model for our fiducial choices agrees with the current direct collapse models. In Figure 16, we show the dark matter merger tree from redshift $z = 27$ to 17 when the first BH is seeded in our simulation. There are 30 dark matter in total with mass above $10^8 M_{\odot}$ that merged between $z = 27$ and 18 . Since we only trace the major branch where the major progenitor is located, this number (30) is quite a conservative estimate. Assuming an occupation fraction of DCBHs between 5% and 10% (DeGraf & Sijacki 2020), the seed BH mass at $z \sim 17$ at least should be $[1.5, 3] \times 10^5 M_{\odot}$, which is slightly above our fiducial choice. Hence, our fiducial choice of BH seed mass is on the slightly conservative side. As a result, the BH mass at $z \sim 6$ could be more massive than our calculation.

However, the implementation of feedback and numerical resolution is likely to be important. It has been documented that BH mass also depends on how the feedback is coupled to the surrounding gas (Wurster & Thacker 2013; Zubovas et al. 2016). In addition, numerical resolution could potentially play an important role (Bourne et al. 2015). The BH mass in our high resolution is slightly lower than that in the low-resolution run. It is beyond the scope of this paper to study the impact of various implementations of feedback and resolution effects.

In addition, the stellar mass of the host galaxy also contains some uncertainties. Essentially, we are extrapolating the wind scaling relations used in our previous work (Zhu & Li 2016), which works well for Milky Way-sized galaxies at $z = 0$, to this extremely massive system at high- z . We use a local dark matter velocity dis-

person (around 60 dark matter particles) as a proxy to estimate the wind velocity as in Vogelsberger et al. (2013). Recently, Pillepich et al. (2018a) has shown that this estimate introduces a redshift dependence. If the wind injection velocity and the wind mass load factor are increased similarly as in our simulation, one might expect that the stellar mass of the host galaxy will be reduced.

5.3 Comparison with Previous Zoom-in Quasar Simulations

Sijacki et al. (2009) performed a set of 6 zoom-in re-simulations of the most massive halo with a mass $10^{13} M_{\odot}$ at $z = 6$ from the Millennium simulation with various resolutions, using the conventional BH recipes ($10^{5-6} M_{\odot}$ seed in $10^9 - 10^{10} M_{\odot}$ halo) but also including BH gravitational recoil. They produced a $10^9 M_{\odot}$ SMBH at $z \sim 6$. They also found that resolution did not have a significant effect on the final BH mass. For example, the final BH mass differed by only a factor of ~ 1.5 between the lowest- resolution simulation and the highest-resolution one when the resolution was increased by a factor of 8.

Feng et al. (2014) used zoom-in SPH simulations of three high-redshift quasars from $10^{12}-10^{13} M_{\odot}$ halos at $z \sim 6$ in the MassiveBlack simulation to examine cold flows as a viable feeding mechanism of high- z quasars (Di Matteo et al. 2012). They show that the result of a $10^9 M_{\odot}$ BH at $z \sim 7$ seen in the uni-grid simulation, which was presented in Di Matteo et al. (2012), is quite insensitive to numerical resolution, feedback prescriptions or SPH formulations (conventional SPH vs. pressure-entropy by Hopkins 2013). At high- z , cold streams of gas from the cosmic web are able to directly feed the central BHs undisrupted by the feedback from accreting BHs.

Dubois et al. (2013) simulated a slightly less massive halo ($5 \times 10^{11} M_{\odot}$) at $z \sim 6$ using the RAMSES code. They found that cold filamentary gas fuels rapid Eddington-limited accretion in the early stages and the BH accretion is maintained both by smooth gas inflow and clump migration within gas disks once the feedback energy is sufficiently large to unbind and remove the cold gas. Also, the stellar-bulge mass content in the host galaxy is altered as the result of AGN feedback. The final BH mass at $z = 6$ is $8 \times 10^7 M_{\odot}$, which is not consistent with billion-solar-mass BHs. However, this mass depends on the host halo mass as well as the adopted feedback efficiency.

Costa et al. (2014) used the moving-mesh code AREPO to simulate 18 dark matter halos from the Millennium simulation (Springel et al. 2005b) including the six most massive halos at $z = 6.1$. BH accretion in these regions proceeds at a much faster rate than the average region. At $z = 6.1$, the most massive BHs have already grown to $\sim 10^9 M_{\odot}$ while the BHs in the average region are $\sim 10^6 M_{\odot}$. In their model, they found that galactic winds from supernova feedback are also crucial to reduce the rapid stellar mass build-up, in general, to reconcile with the observed galaxy numbers in the $z \sim 6$ quasars’ neighboring region (e.g., Kim et al. 2009; Simpson et al. 2014). Feedback from BHs is able to drive a large amount of cold gas with a velocity faster than 1000 km s^{-1} (Costa et al. 2015), which is similar to what is observed in velocity width distributions.

Curtis & Sijacki (2016a) studied an $8 \times 10^{12} M_{\odot}$ halo at $z = 5$ using the AREPO code. Regions around BHs are refined using the super-Lagrangian refinement method in Curtis & Sijacki (2015). A massive rotationally supported gas disk is found in the presence of a $\sim 10^9 M_{\odot}$ central BH. In comparison, the cold gas disk is otherwise not present without the refinement method.

Smidt et al. (2018) implemented X-ray photon transportation into the hydrodynamics and chemistry network of ENZO and used it to simulate a $10^{12} M_{\odot}$ halo at $z = 7$ without prior major merger

history. They reported that a black hole fed by cold gas streams, seeded at $z \sim 20$ with $10^5 M_\odot$, is able to grow to a supermassive BH with $2.15 \times 10^9 M_\odot$ at $z \sim 7$.

Huang et al. (2020) carried out three zoom-in simulations of the same halo from the BlueTides simulation with different seed masses of 5×10^3 , 5×10^4 , and $5 \times 10^5 M_\odot$ while keeping the halo to BH mass ratio fixed. They found that the BH mass converges to $\sim 10^9 M_\odot$ by $z=6$ regardless of the seeding procedure while their early growth histories at $z > 10$ differ. The Eddington-limited accretion between $z = 10$ and 6 within gas-rich environments, until the BH feedback sets in, is in good agreement with what we have found. The constrained realization of the Gaussian field they employed appears to be a promising way to simulate rare density peaks at high z , within a small periodic box of $\sim 15\text{Mpc}$, similar to the zoom-in region in our study.

The role of cold accretion in feeding the first quasars was noted by Di Matteo et al. (2012), although the low resolution of the simulations and (possible) SPH artifacts may affect the dynamics of cold accretion and its interaction between hot halo gas and dense star-forming gas (e.g., Nelson et al. 2013). Our simulation offers a more detailed view of the gas distribution around the first quasar thanks to its higher spatial resolution and the use of GIZMO for a better performance in fluid mixing than the SPH code (see Hopkins 2015). This is an improvement step forward to bridging the scale of cosmological gas accretion to the central BH scale.

5.4 Comparison with Previous Works on Super-critical Accretion

Super-critical accretion through a slim disk provides a viable route for rapid mass growth of light BH seeds into high- z quasars (Madau et al. 2014; Volonteri et al. 2015). Madau et al. (2014) have argued that a moderate super-Eddington ratio $\sim 3\text{--}4$ is able to grow a $100 M_\odot$ stellar mass BHs to a $10^9 M_\odot$ BH before $z = 6$. Using simulations with the RAMSES and GIZMO codes, Lupi et al. (2016) simulated the growth of BHs using a super-critical accretion model. They employ a star formation and feedback model with delayed cooling and the AGN thermal feedback model of Dubois et al. (2014). In their low-resolution runs, super-critical accretion is able to increase BH masses from $100 M_\odot$ to $10^4 M_\odot$ within a rapid Myr timescale, which is much faster than the standard thin accretion disk model. In their high-resolution runs, the growth rates of the BH mass are both reduced significantly in the thin accretion disk and slim-disk accretion models. Note that, the accretion rate estimate in Lupi et al. (2016) estimates the mass flux rate within a prescribed accretion zone, which is different from Bondi-like accretion.

Due to the different models and their implementations in Lupi et al. (2016), it is difficult to directly compare their results with ours. In Lupi et al. (2016), BH accretion is halted once the feedback energy from SNe and BHs creates a hot bubble. In their high resolution run with $\epsilon_r = 0.1$, the feedback energy is strong enough such that the BH mass barely grows within 3 Myr. The most efficient growth of BHs occurs when they are embedded in cold gas, which could be the result of replenishment of cold gas from large scale filaments and mergers. A maximum Eddington ratio of 500 in their simulation enables a brief episode of rapid mass growth.

In our simulation, the accretion of cold gas is modeled within the two-phase ISM model. Any thermal feedback from BH accretion is immediately distributed around the neighboring gas particles. As a result, the effect of BH feedback is not solved explicitly in the cold/hot gas phase. The effect of feedback appears to be strong as indicated by the large oscillations in the mass accretion rate

before $z = 14$ shown in Figure 6. This approach is less sensitive to numerical resolution, as discussed in the previous sections. As a result, the boost of mass growth rate with the super-critical accretion in our simulation is quite modest. There is one advantageous feature of the super-critical accretion model though, in that it is able to grow a $10^{10} M_\odot$ BH at $z \sim 6$ while not affecting the majority of the less massive BHs. However, when BHs are spun up due to coherent flows with a large duty cycle (Volonteri et al. 2013), the final BH mass is even closer to our fiducial model.

We are mindful that the simulation results depend strongly on the physical models and numerical methods. We note that the different BH accretion model in the Simba simulation assumes that the rate scales linearly with the gas inflow rate, which may significantly boost the BHAR and make it easier for small BH seeds to grow more quickly. However, the observations suggest that the $z \sim 6$ quasars they do not follow a linear BHAR–SFR correlation (Venemans et al. 2018), and that they do not follow the same $M_{\text{BH}} - M_\star$ correlation as local galaxies (Pensabene et al. 2020) as produced by the Simba simulation. Our simulations show broad agreement with observations of $z \sim 6$, which is encouraging, but more work is needed to fully unravel the BH accretion and star formation at high redshifts.

6 CONCLUSIONS

We have performed a suite of 15 cosmological zoom-in simulations to test models of the formation of early quasars. We chose the most massive halo from a $\sim \text{Gpc}^3$ volume, which has a mass of $\sim 10^{13} M_\odot$ at $z = 6$ and a history of multiple major mergers. We test BH seeds of $10^1 - 10^6 M_\odot$, and different accretion and feedback models including both radiatively-efficient thin-disk and super-critical slim-disk accretion. Here is a summary of our findings:

- Abundant gas supply and efficient angular momentum transport by gravitational torques is critical to black hole growth and star formation of the quasars, but the eventual black hole mass depends strongly on the seed mass and radiative efficiency.
- In our fiducial model with Eddington-limited thin-disk accretion, a $10^5 M_\odot$ BH seed planted in the host halo of $10^{10} M_\odot$ at $z \sim 19$ can grow to $\sim 7 \times 10^8 M_\odot$ at $z \sim 7.5$, resembling the SMBH of ULAS J1342+0928, currently the most distant quasar at $z = 7.54$, and to $\sim 4 \times 10^9 M_\odot$ at $z \sim 6$, consistent with the majority of luminous quasars in that epoch.
- Light or intermediate seeds of $\lesssim 10^4 M_\odot$ fail to grow to $10^9 M_\odot$ by $z \sim 6$ despite super-critical accretion, while heavy seeds of $\gtrsim 10^5 M_\odot$ in $10^{10} M_\odot$ halos can in both thin- and slim-disk models, provided that the duty cycle of near-Eddington accretion with an Eddington ratio $\lambda_{\text{Edd}} \gtrsim 0.6$ is maintained at $\gtrsim 40\%$.
- A hyper-Eddington model with $\lambda_{\text{Edd}} \gg 1$, rather than boosting BH growth, suffers from dramatically reduced accretion because of strong feedback to produce $\sim 10^9 M_\odot$ SMBHs by $z \sim 6$, while near-Eddington or moderately super-Eddington accretion produces more massive BHs than the former by two orders of magnitude.
- The super-critical model may lead to moderate super-Eddington accretion with $\lambda_{\text{Edd}} \lesssim 3$ for low-spin BHs due to low radiative efficiency $\sim 10^{-4} \lesssim \epsilon_r \lesssim 0.1$, which facilitates rapid BH growth. However, for high-spin BHs, the advantage is diminished sharply by increased radiative feedback. A $10^5 M_\odot$ BH seed can grow to $\sim 8 \times 10^9 M_\odot$ by $z \sim 6$ under super-critical accretion with no spin, but only to $\sim 6 \times 10^8 M_\odot$ if it spins maximally.

- Most of the BH mass is assembled through gas accretion of the main progenitor other than through the merger of the less massive BHs. There is good agreement on the BH mass among various Bondi accretion models, as the BH growth is largely dominated by the Eddington-accretion phase.

- The quasar host galaxy experiences strong starbursts with star formation rates of $10^2 - 10^3 M_{\odot}/\text{yr}$ triggered by violent galaxy interactions. The host galaxy is massive with a stellar mass of $5.9 \times 10^{11} M_{\odot}$, yet it is highly compact, with 2/3 of the stellar mass concentrating within 2.5 kpc from the galaxy center.

Overall, our simulations show that the first $10^8 - 10^9 M_{\odot}$ SMBHs can grow from heavy seeds of $\geq 10^4 M_{\odot}$ via rapid, self-regulated accretion booted by gas-rich mergers, even though we employ much stronger galactic feedback akin to the outflow model in the Illustris simulation than that in the Li et al. (2007) simulation. This suggests that the BH seeds play a critical role in the growth of SMBHs, and that more observations and theoretical works are needed to identify the formation mechanisms of potential heavy BH seeds and their subsequent evolution.

ACKNOWLEDGMENTS

We thank Phil Hopkins for a private version of GIZMO code, and we thank Marta Volonteri, Rosa Valiante, Laura Pentericci and Luca Graziani for valuable discussions. QZ is supported by the McWilliams Fellowship from The McWilliams Center for Cosmology at Carnegie Mellon University. YL acknowledges support from NSF grants AST-1412719 and MRI-1626251. YL and RS acknowledge support from the Amaldi Research Center funded by the MIUR program “Dipartimento di Eccellenza” (CUP:B81I18001170001), and from the INFN TEONGRAV specific initiative. HY acknowledges support from MEXT/JSPS KAKENHI Grant Number 17H04827, 20H04724, and NAOJ ALMA Scientific Research Grant Numbers 2019-11A. The numerical computations and data analysis in this paper have been carried out on the CyberLAMP cluster supported by MRI-1626251, operated and maintained by the Institute for CyberScience at the Pennsylvania State University. The Institute for Gravitation and the Cosmos is supported by the Eberly College of Science and the Office of the Senior Vice President for Research at the Pennsylvania State University.

DATA AVAILABILITY

The data generated in this research will be shared on reasonable request to the corresponding author.

REFERENCES

Abramowicz M. A., Fragile P. C., 2013, *Living Reviews in Relativity*, **16**, 1
 Abramowicz M. A., Czerny B., Lasota J. P., Szuszkiewicz E., 1988, *ApJ*, **332**, 646
 Agarwal B., Khochfar S., Johnson J. L., Neistein E., Dalla Vecchia C., Livio M., 2012, *MNRAS*, **425**, 2854
 Agarwal B., Davis A. J., Khochfar S., Natarajan P., Dunlop J. S., 2013, *MNRAS*, **432**, 3438
 Agertz O., et al., 2007, *MNRAS*, **380**, 963
 Alvarez M. A., Wise J. H., Abel T., 2009, *ApJ*, **701**, L133
 Anglés-Alcázar D., Davé R., Faucher-Giguère C.-A., Özel F., Hopkins P. F., 2017, *MNRAS*, **464**, 2840
 Bañados E., et al., 2016, *ApJS*, **227**, 11

Bañados E., et al., 2018, *Nature*, **553**, 473
 Barnes J. E., Hernquist L., 1996, *ApJ*, **471**, 115
 Bauer A., Springel V., 2012, *MNRAS*, **423**, 2558
 Becerra F., Greif T. H., Springel V., Hernquist L. E., 2015, *MNRAS*, **446**, 2380
 Becerra F., Marinacci F., Bromm V., Hernquist L. E., 2018, *MNRAS*, **480**, 5029
 Begelman M. C., Volonteri M., Rees M. J., 2006, *MNRAS*, **370**, 289
 Bekenstein J. D., 1973, *ApJ*, **183**, 657
 Blecha L., Loeb A., 2008, *MNRAS*, **390**, 1311
 Blecha L., Cox T. J., Loeb A., Hernquist L., 2011, *MNRAS*, **412**, 2154
 Bondi H., Hoyle F., 1944, *MNRAS*, **104**, 273
 Booth C. M., Schaye J., 2009, *MNRAS*, **398**, 53
 Bourne M. A., Zubovas K., Nayakshin S., 2015, *MNRAS*, **453**, 1829
 Bromm V., Loeb A., 2003, *ApJ*, **596**, 34
 Calura F., Gilli R., Vignali C., Pozzi F., Pipino A., Matteucci F., 2014, *MNRAS*, **438**, 2765
 Chon S., Hosokawa T., 2019, *MNRAS*, **488**, 2658
 Chon S., Hosokawa T., Yoshida N., 2018, *MNRAS*, **475**, 4104
 Costa T., Sijacki D., Trenti M., Haehnelt M. G., 2014, *MNRAS*, **439**, 2146
 Costa T., Sijacki D., Haehnelt M. G., 2015, *MNRAS*, **448**, L30
 Crain R. A., et al., 2015, *MNRAS*, **450**, 1937
 Curtis M., Sijacki D., 2015, *MNRAS*, **454**, 3445
 Curtis M., Sijacki D., 2016a, *MNRAS*, **457**, L34
 Curtis M., Sijacki D., 2016b, *MNRAS*, **463**, 63
 Davé R., Anglés-Alcázar D., Narayanan D., Li Q., Rafieferantsoa M. H., Appleby S., 2019, *MNRAS*, **486**, 2827
 Davies F. B., Hennawi J. F., Eilers A.-C., 2019, *ApJ*, **884**, L19
 Davis M., Efstathiou G., Frenk C. S., White S. D. M., 1985, *ApJ*, **292**, 371
 DeGraf C., Sijacki D., 2020, *MNRAS*, **491**, 4973
 Decarli R., et al., 2018, *ApJ*, **854**, 97
 Di Matteo T., Springel V., Hernquist L., 2005, *Nature*, **433**, 604
 Di Matteo T., Colberg J., Springel V., Hernquist L., Sijacki D., 2008, *ApJ*, **676**, 33
 Di Matteo T., Khandai N., DeGraf C., Feng Y., Croft R. A. C., Lopez J., Springel V., 2012, *ApJ*, **745**, L29
 Dolag K., Komatsu E., Sunyaev R., 2016, *MNRAS*, **463**, 1797
 Dubois Y., Devriendt J., Teyssier R., Slyz A., 2011, *MNRAS*, **417**, 1853
 Dubois Y., Pichon C., Haehnelt M., Kimm T., Slyz A., Devriendt J., Pogosyan D., 2012, *MNRAS*, **423**, 3616
 Dubois Y., Pichon C., Devriendt J., Silk J., Haehnelt M., Kimm T., Slyz A., 2013, *MNRAS*, **428**, 2885
 Dubois Y., et al., 2014, *MNRAS*, **444**, 1453
 Eggen O. J., Lynden-Bell D., Sandage A. R., 1962, *ApJ*, **136**, 748
 Fan X., et al., 2001, *AJ*, **122**, 2833
 Faucher-Giguère C.-A., Kereš D., Dijkstra M., Hernquist L., Zaldarriaga M., 2010, *ApJ*, **725**, 633
 Feng Y., Di Matteo T., Croft R., Khandai N., 2014, *MNRAS*, **440**, 1865
 Feng Y., Di-Matteo T., Croft R. A., Bird S., Battaglia N., Wilkins S., 2016, *MNRAS*, **455**, 2778
 Ferrara A., Salvadori S., Yue B., Schleicher D., 2014, *MNRAS*, **443**, 2410
 Freitag M., Rasio F. A., Baumgardt H., 2006a, *MNRAS*, **368**, 121
 Freitag M., Gürkan M. A., Rasio F. A., 2006b, *MNRAS*, **368**, 141
 Fukushima H., Hosokawa T., Chiaki G., Omukai K., Yoshida N., Kuiper R., 2020, *MNRAS*, **497**, 829
 Gaspari M., Ruszkowski M., Oh S. P., 2013, *MNRAS*, **432**, 3401
 Gaspari M., Brighenti F., Temi P., 2015, *A&A*, **579**, A62
 Genel S., et al., 2014, *MNRAS*, **445**, 175
 Genzel R., et al., 2010, *MNRAS*, **407**, 2091
 Glazebrook K., et al., 2017, *Nature*, **544**, 71
 Glover S. C. O., 2015a, *MNRAS*, **451**, 2082
 Glover S. C. O., 2015b, *MNRAS*, **453**, 2901
 Greene J. E., Strader J., Ho L. C., 2020, *ARA&A*, **58**, 257
 Haemmerlé L., Mayer L., Klessen R. S., Hosokawa T., Madau P., Bromm V., 2020, *Space Sci. Rev.*, **216**, 48
 Hahn O., Abel T., 2011, *MNRAS*, **415**, 2101
 Hirano S., Bromm V., 2017, *MNRAS*, **470**, 898
 Ho L. C., 2007, *ApJ*, **669**, 821

- Hopkins P. F., 2013, *MNRAS*, **428**, 2840
- Hopkins P. F., 2015, *MNRAS*, **450**, 53
- Hopkins P. F., Quataert E., 2010, *MNRAS*, **407**, 1529
- Hopkins P. F., Torrey P., Faucher-Giguère C.-A., Quataert E., Murray N., 2016, *MNRAS*, **458**, 816
- Huang K.-W., Ni Y., Feng Y., Di Matteo T., 2020, *MNRAS*, **496**, 1
- Inayoshi K., Haiman Z., 2016, *ApJ*, **828**, 110
- Inayoshi K., Visbal E., Kashiyama K., 2015, *MNRAS*, **453**, 1692
- Inayoshi K., Visbal E., Haiman Z., 2020, *ARA&A*, **58**, 27
- Jeon M., Pawlik A. H., Greif T. H., Glover S. C. O., Bromm V., Milosavljević M., Klessen R. S., 2012, *ApJ*, **754**, 34
- Jiang L., et al., 2016, *ApJ*, **833**, 222
- Johnson J. L., Khochfar S., Greif T. H., Durier F., 2011, *MNRAS*, **410**, 919
- Katz H., Sijacki D., Haehnelt M. G., 2015, *MNRAS*, **451**, 2352
- Kaviraj S., et al., 2017, *MNRAS*, **464**, 3131
- Khandai N., Feng Y., DeGraf C., Di Matteo T., Croft R. A. C., 2012, *MNRAS*, **423**, 2397
- Khandai N., Di Matteo T., Croft R., Wilkins S., Feng Y., Tucker E., DeGraf C., Liu M.-S., 2015, *MNRAS*, **450**, 1349
- Kim S., et al., 2009, *ApJ*, **695**, 809
- Komatsu E., et al., 2009, *ApJS*, **180**, 330
- Kormendy J., Ho L. C., 2013, *ARA&A*, **51**, 511
- Latif M. A., Ferrara A., 2016, *Publ. Astron. Soc. Australia*, **33**, e051
- Lauer T. R., Tremaine S., Richstone D., Faber S. M., 2007, *ApJ*, **670**, 249
- Leitherer C., et al., 1999, *ApJS*, **123**, 3
- Leitherer C., et al., 2011, Starburst99: Synthesis Models for Galaxies with Active Star Formation (ascl:1104.003)
- Leroy A. K., Walter F., Brinks E., Bigiel F., de Blok W. J. G., Madore B., Thornley M. D., 2008, *AJ*, **136**, 2782
- Li Y., et al., 2007, *ApJ*, **665**, 187
- Li Y., et al., 2008, *ApJ*, **678**, 41
- Luo Y., Shlosman I., Nagamine K., Fang T., 2020, *MNRAS*, **492**, 4917
- Lupi A., Haardt F., Dotti M., Fiacconi D., Mayer L., Madau P., 2016, *MNRAS*, **456**, 2993
- Lupi A., Volonteri M., Decarli R., Bovino S., Silk J., Bergeron J., 2019, *MNRAS*, **488**, 4004
- Madau P., Haardt F., Dotti M., 2014, *ApJ*, **784**, L38
- Marchesini D., et al., 2010, *ApJ*, **725**, 1277
- Matsuoka Y., et al., 2018, *ApJ*, **869**, 150
- Matsuoka Y., et al., 2019, *ApJ*, **872**, L2
- Mayer L., Bonoli S., 2019, *Reports on Progress in Physics*, **82**, 016901
- Mayer L., Kazantzidis S., Escala A., Callegari S., 2010, *Nature*, **466**, 1082
- Mazzucchelli C., Bañados E., Decarli R., Farina E. P., Venemans B. P., Walter F., Overzier R., 2017, *ApJ*, **834**, 83
- Mobasher B., et al., 2005, *ApJ*, **635**, 832
- Mortlock D. J., et al., 2011, *Nature*, **474**, 616
- Muratov A. L., Kereš D., Faucher-Giguère C.-A., Hopkins P. F., Quataert E., Murray N., 2015, *MNRAS*, **454**, 2691
- Narayan R., Salšowski A., Soria R., 2017, *MNRAS*, **469**, 2997
- Negri A., Volonteri M., 2017, *MNRAS*, **467**, 3475
- Nelson D., Vogelsberger M., Genel S., Sijacki D., Kereš D., Springel V., Hernquist L., 2013, *MNRAS*, **429**, 3353
- Onoue M., et al., 2019, *ApJ*, **880**, 77
- Pacucci F., Volonteri M., Ferrara A., 2015, *MNRAS*, **452**, 1922
- Pacucci F., Natarajan P., Volonteri M., Cappelluti N., Urry C. M., 2017, *ApJ*, **850**, L42
- Pelupessy F. I., Di Matteo T., Ciardi B., 2007, *ApJ*, **665**, 107
- Pensabene A., Carniani S., Perna M., Cresci G., Decarli R., Maiolino R., Marconi A., 2020, *A&A*, **637**, A84
- Pezzulli E., Valiante R., Schneider R., 2016, *MNRAS*, **458**, 3047
- Pezzulli E., Valiante R., Orofino M. C., Schneider R., Gallerani S., Sbarrato T., 2017, *MNRAS*, **466**, 2131
- Pillepich A., et al., 2018a, *MNRAS*, **473**, 4077
- Pillepich A., et al., 2018b, *MNRAS*, **475**, 648
- Planck Collaboration et al., 2016, *A&A*, **594**, A13
- Portegies Zwart S. F., McMillan S. L. W., 2000, *ApJ*, **528**, L17
- Portegies Zwart S. F., McMillan S. L. W., 2002, *ApJ*, **576**, 899
- Reed S. L., et al., 2017, *MNRAS*, **468**, 4702
- Rees M. J., 1978, *Phys. Scr.*, **17**, 193
- Regan J. A., Visbal E., Wise J. H., Haiman Z., Johansson P. H., Bryan G. L., 2017, *Nature Astronomy*, **1**, 0075
- Regan J. A., Downes T. P., Volonteri M., Beckmann R., Lupi A., Trebitsch M., Dubois Y., 2019, *MNRAS*, **486**, 3892
- Reines A. E., Volonteri M., 2015, *ApJ*, **813**, 82
- Ricarte A., Natarajan P., 2018, *MNRAS*, **481**, 3278
- Ryu T., Tanaka T. L., Perna R., Haiman Z., 2016, *MNRAS*, **460**, 4122
- Sakurai Y., Yoshida N., Fujii M. S., Hirano S., 2017, *MNRAS*, **472**, 1677
- Sądowski A., 2009, *ApJS*, **183**, 171
- Sądowski A., Lasota J.-P., Abramowicz M. A., Narayan R., 2016, *MNRAS*, **456**, 3915
- Schaye J., et al., 2015, *MNRAS*, **446**, 521
- Shakura N. I., Sunyaev R. A., 1973, *A&A*, **24**, 337
- Shen Y., et al., 2019, *ApJ*, **873**, 35
- Sijacki D., Springel V., Di Matteo T., Hernquist L., 2007, *MNRAS*, **380**, 877
- Sijacki D., Springel V., Haehnelt M. G., 2009, *MNRAS*, **400**, 100
- Sijacki D., Vogelsberger M., Genel S., Springel V., Torrey P., Snyder G. F., Nelson D., Hernquist L., 2015, *MNRAS*, **452**, 575
- Simpson C., Mortlock D., Warren S., Cantalupo S., Hewett P., McLure R., McMahon R., Venemans B., 2014, *MNRAS*, **442**, 3454
- Sądowski A., 2009, *ApJS*, **183**, 171
- Smidt J., Whalen D. J., Johnson J. L., Surace M., Li H., 2018, *ApJ*, **865**, 126
- Smith B. D., Wise J. H., O'Shea B. W., Norman M. L., Khochfar S., 2015, *MNRAS*, **452**, 2822
- Smith B. D., et al., 2017, *MNRAS*, **466**, 2217
- Smith B. D., Regan J. A., Downes T. P., Norman M. L., O'Shea B. W., Wise J. H., 2018, *MNRAS*, **480**, 3762
- Soltan A., 1982, *MNRAS*, **200**, 115
- Spergel D. N., et al., 2003, *ApJS*, **148**, 175
- Springel V., Hernquist L., 2003, *MNRAS*, **339**, 289
- Springel V., Di Matteo T., Hernquist L., 2005a, *MNRAS*, **361**, 776
- Springel V., et al., 2005b, *Nature*, **435**, 629
- Springel V., et al., 2018, *MNRAS*, **475**, 676
- Stacy A., Bromm V., Lee A. T., 2016, *MNRAS*, **462**, 1307
- Stefanon M., et al., 2015, *ApJ*, **803**, 11
- Steinhardt C. L., Capak P., Masters D., Speagle J. S., 2016, *ApJ*, **824**, 21
- Sugimura K., Hosokawa T., Yajima H., Omukai K., 2017, *MNRAS*, **469**, 62
- Sugimura K., Matsumoto T., Hosokawa T., Hirano S., Omukai K., 2020, *ApJ*, **892**, L14
- Tagawa H., Haiman Z., Kocsis B., 2020, *ApJ*, **892**, 36
- Takeo E., Inayoshi K., Ohsuga K., Takahashi H. R., Mineshige S., 2019, *MNRAS*, **488**, 2689
- Tanaka T., Haiman Z., 2009, *ApJ*, **696**, 1798
- Tanaka T., Perna R., Haiman Z., 2012, *MNRAS*, **425**, 2974
- Tenneti A., Wilkins S. M., Di Matteo T., Croft R. A. C., Feng Y., 2019, *MNRAS*, **483**, 1388
- Thomas N., Davé R., Anglés-Alcázar D., Jarvis M., 2019, *MNRAS*, **487**, 5764
- Tohline J. E., Simonson G. F., Caldwell N., 1982, *ApJ*, **252**, 92
- Townsend R. H. D., 2009, *ApJS*, **181**, 391
- Tremblay G. R., et al., 2016, *Nature*, **534**, 218
- Valiante R., Schneider R., Salvadori S., Gallerani S., 2014, *MNRAS*, **444**, 2442
- Valiante R., Schneider R., Volonteri M., Omukai K., 2016, *MNRAS*, **457**, 3356
- Valiante R., Agarwal B., Habouzit M., Pezzulli E., 2017, *Publ. Astron. Soc. Australia*, **34**, e031
- Venemans B. P., et al., 2015, *MNRAS*, **453**, 2259
- Venemans B. P., et al., 2018, *ApJ*, **866**, 159
- Vito F., et al., 2019, *A&A*, **630**, A118
- Vogelsberger M., Genel S., Sijacki D., Torrey P., Springel V., Hernquist L., 2013, *MNRAS*, **436**, 3031
- Vogelsberger M., et al., 2014a, *MNRAS*, **444**, 1518
- Vogelsberger M., et al., 2014b, *MNRAS*, **444**, 1518
- Vogelsberger M., et al., 2014c, *Nature*, **509**, 177

- Volonteri M., 2010, [A&ARv](#), **18**, 279
- Volonteri M., Bellocvary J., 2012, [Reports on Progress in Physics](#), **75**, 124901
- Volonteri M., Rees M. J., 2006, [ApJ](#), **650**, 669
- Volonteri M., Stark D. P., 2011, [MNRAS](#), **417**, 2085
- Volonteri M., Sikora M., Lasota J.-P., Merloni A., 2013, [ApJ](#), **775**, 94
- Volonteri M., Silk J., Dubus G., 2015, [ApJ](#), **804**, 148
- Wang R., et al., 2010, [ApJ](#), **714**, 699
- Wang R., et al., 2013, [ApJ](#), **773**, 44
- Wang F., et al., 2019, [ApJ](#), **884**, 30
- Weinberger R., et al., 2017, [MNRAS](#), **465**, 3291
- Weinberger R., et al., 2018, [MNRAS](#), **479**, 4056
- Wiklund T., Dickinson M., Ferguson H. C., Gialvalisco M., Mobasher B., Goggin N. A., Panagia N., 2008, [ApJ](#), **676**, 781
- Willott C. J., et al., 2010, [AJ](#), **139**, 906
- Wise J. H., Regan J. A., O'Shea B. W., Norman M. L., Downes T. P., Xu H., 2019, [Nature](#), **566**, 85
- Woods T. E., Heger A., Whalen D. J., Haemmerlé L., Klessen R. S., 2017, [ApJ](#), **842**, L6
- Woods T. E., et al., 2019, [Publ. Astron. Soc. Australia](#), **36**, e027
- Wu X.-B., et al., 2015, [Nature](#), **518**, 512
- Wurster J., Thacker R. J., 2013, [MNRAS](#), **431**, 2513
- Yajima H., Khochfar S., 2016, [MNRAS](#), **457**, 2423
- Yang J., et al., 2019, [AJ](#), **157**, 236
- Yang J., et al., 2020, [ApJ](#), **897**, L14
- Yi W.-M., et al., 2014, [ApJ](#), **795**, L29
- Zhu Q., Li Y., 2016, [ApJ](#), **831**, 52
- Zhu Q., Hernquist L., Li Y., 2015, [ApJ](#), **800**, 6
- Zhu Q., Smith B., Hernquist L., 2017, [MNRAS](#), **470**, 1017
- Zubovas K., Bourne M. A., Nayakshin S., 2016, [MNRAS](#), **457**, 496
- van de Voort F., Davis T. A., Kereš D., Quataert E., Faucher-Giguère C.-A., Hopkins P. F., 2015, [MNRAS](#), **451**, 3269

This paper has been typeset from a \LaTeX file prepared by the author.